

Review

Semiconductors Application Forms and Doping Benefits to Wastewater Treatment: A Comparison of TiO_2 , WO_3 , and $g\text{-C}_3\text{N}_4$

Eryk Fernandes ^{*}, João Gomes  and Rui C. Martins 

University of Coimbra, CIEQP—Chemical Engineering Processes and Forest Products Research Center, Department of Chemical Engineering, Faculty of Sciences and Technology, Rua Silvio Lima, Polo II, 3030-790 Coimbra, Portugal

* Correspondence: eryk@eq.uc.pt; Tel.: +351-239798723; Fax: +351-239798

Abstract: Photocatalysis has been vastly applied for the removal of contaminants of emerging concern (CECs) and other micropollutants, with the aim of future water reclamation. As a process based upon photon irradiation, materials that may be activated through natural light sources are highly pursued, to facilitate their application and reduce costs. TiO_2 is a reference material, and it has been greatly optimized. However, in its typical configuration, it is known to be mainly active under ultraviolet radiation. Thus, multiple alternative visible light driven (VLD) materials have been intensively studied recently. WO_3 and $g\text{-C}_3\text{N}_4$ are currently attractive VLD catalysts, with WO_3 possessing similarities with TiO_2 as a metal oxide, allowing correlations between the knowledge regarding the reference catalyst, and $g\text{-C}_3\text{N}_4$ having an interesting and distinct non-metallic polymeric structure with the benefit of easy production. In this review, recent developments towards CECs degradation in TiO_2 based photocatalysis are discussed, as reference catalyst, alongside the selected alternative materials, WO_3 and $g\text{-C}_3\text{N}_4$. The aim here is to evaluate the different techniques more commonly explored to enhance catalyst photo-activity, specifically doping with multiple elements and the formation of composite materials. Moreover, the possible combination of photocatalysis and ozonation is also explored, as a promising route to potentialize their individual efficiencies and overcome typical drawbacks.

Keywords: contaminants of emerging concern; catalysts doping; composite materials; visible photocatalysis; ozonation



Citation: Fernandes, E.; Gomes, J.; Martins, R.C. Semiconductors Application Forms and Doping Benefits to Wastewater Treatment: A Comparison of TiO_2 , WO_3 , and $g\text{-C}_3\text{N}_4$. *Catalysts* **2022**, *12*, 1218. <https://doi.org/10.3390/catal12101218>

Academic Editor: Jaime Carbajo

Received: 22 September 2022

Accepted: 8 October 2022

Published: 12 October 2022

Publisher's Note: MDPI stays neutral with regard to jurisdictional claims in published maps and institutional affiliations.



Copyright: © 2022 by the authors. Licensee MDPI, Basel, Switzerland. This article is an open access article distributed under the terms and conditions of the Creative Commons Attribution (CC BY) license (<https://creativecommons.org/licenses/by/4.0/>).

1. Introduction

Society and industry are subject to constant evolution and increasing complexity. Consequently, the consumption of crucial resources for their expansion also progressively grows. Water, as the most vital of these resources, becomes an endangered commodity, making the discussion regarding its renewability against the growing usage and degradation a high-interest topic. Fresh and drinkable water scarcity is caused by different factors, such as climate change, loss of biodiversity, and pollution, which can be due to the direct irregular disposal of sewage, effluents, and other contaminated sources into water bodies, or by the inefficient treatment of those in wastewater treatment plants (WWTPs) [1]. Nowadays, an estimated 1.2 billion people live in locations facing water scarcity and 780 million have no access to basic water services, resulting in a variety of diseases associated with contaminated water consumption [2].

The WWTPs are currently responsible for the provision of proper sanitary living conditions for more than 5.2 billion people, but as industries evolve, a large number of different products and chemicals are consumed by the population, eventually making their way into these facilities, which are not designed to treat them [3,4]. There is a great number of these pollutants, but a certain group is particularly important, the contaminants of emerging

concern (CECs), which are a variety of chemicals, such as pesticides, pharmaceutical and personal care products (PPCPs), hormones, and stabilizers [5]. Due to their ineffectiveness, WWTPs become a major source of CECs, which may accumulate in the environment and have already been detected, at ng L^{-1} and $\mu\text{g L}^{-1}$ ranges, in surface and groundwater, as well as in remote places, such as high-altitude rivers and the Antarctic Peninsula [6–9].

Different treatments and techniques have been researched by the scientific community to solve the problem associated with CECs, but a feasible and broad-range solution is yet to be found [10]. Advanced oxidation processes (AOPs) are presented as suitable alternatives for the degradation of a wide range of pollutants, based upon the formation of reactive oxidative species (ROS), most importantly hydroxyl radicals ($\cdot\text{OH}$). AOPs include an array of treatments, vastly explored towards CECs abatements, such as ultraviolet-, ozone-, photocatalysis-, Fenton-, and sulfate-based processes [11–14] (Figure 1). Ozone-based water disinfection treatments are well-established, but also currently one of the most applied AOP for micropollutants removal, being already implemented as tertiary wastewater treatment in some countries [15].

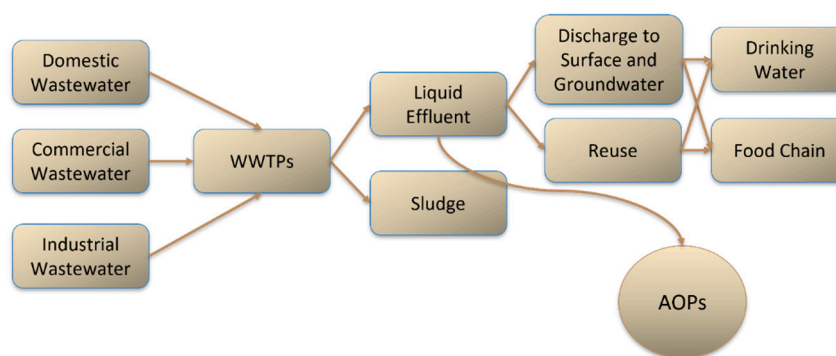


Figure 1. Water treatment scheme and routes of contaminants introduction in the environment.

Ozone is a very strong oxidant, with a redox potential of 2.08 eV, capable of directly reacting with microorganisms and different organic compounds, but it may also be responsible for indirect reactions, producing hydroxyl radicals, which then can interact with the microcontaminants [16]. Nevertheless, this process faces some disadvantages, namely the low solubility of ozone in water, the high energy requirement for its production, low mineralization, and the formation of byproducts potentially more toxic than the parent compounds [17,18]. To enhance the single ozone process, a very common strategy is to integrate or couple it with other AOPs, for instance, O_3/UV , $\text{O}_3/\text{H}_2\text{O}_2$, O_3/Cl , and $\text{O}_3/\text{Photocatalysis}$ [11,19,20]. Photocatalytic ozonation is then a promising combined technique, boosting the treatment efficacy and suppressing the individual processes' disadvantages. Photocatalysis is based upon the activation of a catalyst through photon absorption, which then promotes multiple radical's production reactions that attack a large range of contaminants. The contaminants may also be eliminated directly by the catalyst through adsorption [14]. The photocatalysis, when in combination with ozone, can promote a higher decomposition of the gas in water, diminishing ozone demand and increasing the production of ROS. Besides, ozone may also enhance photocatalysis by acting as an electron receiver, reducing electron-hole recombination, which is one of the major disadvantages of this process [21].

Photocatalytic systems are very adaptable and, currently, there is a great variety of catalysts available to be used, the most common being TiO_2 . Notwithstanding, TiO_2 presents some disadvantages that challenge its large-scale application, but as these materials are easily tunable, recent studies present multiple adaptations to enhance photocatalysts' performances, such as doping using metal and non-metal elements, immobilization onto other materials, as well as the coupling of different catalysts and materials with distinct natures. Another route is the exploration of alternative catalysts, other than TiO_2 , that

present superior performances over visible/solar radiation, lowering the process overall cost, which nowadays corresponds to a high-interest field of exploration [22].

Regarding other catalysts, visible-light-driven (VLD) materials became the aim of an increasing number of studies, presenting a better and easier alternative regarding their activation. $g\text{-C}_3\text{N}_4$ is a currently very significant catalyst, possessing a metal-free polymeric structure, with simple and very adaptable synthesis methods. Another example, WO_3 , also possesses lower bandgap energy and broader absorption of solar radiation while sharing the metal oxide characteristic of TiO_2 , which allows an easier correlation between possible known mechanisms and adaptations that can be made. These alternative materials, although with interesting light absorption properties, still face some drawbacks, some also found in TiO_2 , such as high electron-hole recombination, low specific surface areas, and improper energy band positions, which hinder the potential of the redox reactions responsible for contaminants elimination.

This current review focuses on the critical analysis of current TiO_2 data as a reference catalyst, and its comparison with VLD materials, $g\text{-C}_3\text{N}_4$ and WO_3 . Graphitic carbon nitride was selected due to its high recent relevance among this group of alternative catalysts, possessing a high density of recent scientific studies and distinct composition, while WO_3 also has appealing features and structures, and may represent an important connection between the broad existent knowledge of TiO_2 and metal oxides, with visible light active catalysts. Advantageously, these materials may also be involved in modification techniques to boost their efficiencies and overcome disadvantages, as will be further discussed, focusing on doping techniques and composite formation.

2. General Features of Catalysts for Photo-based Treatment Processes

Titanium dioxide is certainly the most applied catalyst for photocatalytic water treatment and possesses different crystalline phases, anatase, rutile, and brookite, with anatase having a higher general photocatalytic activity [23]. Degussa P25 is a commercial TiO_2 catalyst, vastly used due to its optimized characteristics, presenting a mixed anatase-rutile crystal phase.

The benchmarked P25 catalyst was applied by Gomes et al. [24] for the degradation of a complex solution of insecticides, namely azoxystrobin, buprofezin, imidacloprid, procymidone, simazine, terbutryn, and thiamethoxam. Under solar radiation for 120 min, Degussa P25 TiO_2 completely removed $100 \mu\text{g L}^{-1}$ of almost all pesticides, excluding thiamethoxam (~90%) and procymidone (~50%). The authors also evaluated the scale-up effect, in a pilot-scale 120 L photoreactor, P25 achieved lower degradation yields, expected due to the larger volume, but still favorable, with removal rates higher than 70% with a photon flux of approximately 8 kJ L^{-1} . Photocatalytic ozonation was also assessed, and the higher production of ROS improved the degradation of the insecticides by more than 80%, while single ozonation had considerably lower removal rates for some contaminants, such as Procymidone (~50%) and Imidacloprid (~50%). However, the high electronic density groups characteristics of the contaminants that promote a fast reaction with molecular ozone still allow a noticeably efficient treatment by the single process.

Even with broad usage, TiO_2 faces compromising disadvantages that challenge its full-scale application. Primarily, its high bandgap energy, ~3.2 eV for anatase and ~3.0 eV for rutile TiO_2 , makes its photoactivation possible only under UV radiation, with $\lambda \leq 390 \text{ nm}$, hampering its activation through sunlight as the UV portion represents only 4–6% [14]. Moreover, TiO_2 also presents a high recombination rate of e^-/h^+ and a weak separation of photocarriers, reducing its photocatalytic activity [25]. Thus, other catalysts have been constantly developed and investigated to overcome the disadvantages of TiO_2 and fulfill the need for a feasible material. In the last years, a few catalysts have been the focus of an increasing number of publications, e.g., $g\text{-C}_3\text{N}_4$ and WO_3 materials, which will be more extensively discussed in this review.

Graphitic carbon nitride ($g\text{-C}_3\text{N}_4$) is a metal-free semiconductor catalyst, with high photochemical stability and photoelectric properties, that can be obtained through the

thermal polymerization of numerous low-price nitrogen-rich organic precursors. It emerges as a promising visible-light-driven photocatalyst, as it possesses a typical absorption edge at 450–470 nm which corresponds to a bandgap energy of approximately 2.7 eV [26]. The graphitic C_3N_4 is the most stable among the multiple allotropic forms of C_3N_4 (e.g., cubic, beta, alpha), due to its particular 2D structure formed by triazine or heptazine rings.

As mentioned, g- C_3N_4 can be synthesized through the polymerization of different precursors, which will intrinsically affect the properties of the photocatalyst. Nguyen et al. [27] evaluated this parameter using dicyandiamide, melamine, urea, and thiourea as g- C_3N_4 precursors. Their physical and optical properties were considerably distinct, with urea-based g- C_3N_4 having noticeably better values, a specific surface area (S_{BET}) more than three times higher than the others ($78.9 \text{ m}^2 \text{ g}^{-1}$), and lower bandgap energy (2.72 eV). The authors also conducted a chemical oxidation treatment over the catalysts, a method used for the exfoliation of g- C_3N_4 , improving their properties, such as the surface area, hydrophilicity, and the addition of reactive functional groups (e.g., hydroxyl). The exfoliation treatment resulted in generally higher S_{BET} , pore density, and a slower recombination rate of the photogenerated electron-hole pairs, indicated by the photoluminescence spectra and electrochemical impedance spectroscopy (EIP). However, the E_{bg} of the treated g- C_3N_4 catalyst was also higher (3.4–3.6 eV), attributed to the exfoliation of the bulk structure into thin layers and the quantum confinement effect. Nonetheless, when applied for methylene blue (MB) photodegradation under visible light, the exfoliated catalyst had a significantly better performance, with urea- and thiourea-based catalysts achieving a complete abatement in 180 min. It is important to mention that the use of thiourea as a precursor also inflicts the addition of sulfur in the catalyst structure, which will be further discussed in the next sections.

The g- C_3N_4 exfoliation may also be obtained through other methods, such as ultrasonication in water or alcohol solutions, or thermal treatment [26]. Fernandes et al. [28] compared Degussa P25 TiO_2 with dicyandiamide-based g- C_3N_4 , subjected to a posterior thermal treatment, for the removal of methyl-, ethyl-, and propylparaben (0.08 mM), individually and in the mixture. Under visible light, the polymeric catalyst achieved complete elimination of parabens within 20 min, individually, and 30 min when in a mixture, while P25 TiO_2 obtained the same results in 120 min. The g- C_3N_4 also proved capable to maintain its stability and efficiency when tested in real water matrices, tap and river water. The thermal exfoliation may also partially remove amino groups and thus introduce defects in the catalyst structure, which reduce electron and hole recombination [29].

The combination of g- C_3N_4 photocatalysis and ozonation is still very minimally investigated, yet some studies have been conducted to demonstrate a propitious tertiary wastewater treatment. The more negative conduction band of g- C_3N_4 , in comparison to TiO_2 , makes it easier for the excited electrons to be captured by ozone. This system was detailed by Orge et al. [29], applying a dicyandiamide as a catalyst precursor with a thermal post-treatment for exfoliation, for the elimination of oxamic acid (OMA), a common by-product of the oxidation of nitrogenous compounds, using a LED system. The exfoliated catalyst, which had an increase of more than 10 times its surface area, presented a much faster removal rate and full elimination of OMA in 120 min, compared with the same system using a benchmark TiO_2 or single ozonation, which resulted in near 80% and 5% removals. Thus, the beneficial synergetic effect was proposed to be due to the interaction between ozone and the graphitic layers of g- C_3N_4 . However, in the catalyst's reusing evaluation, the authors indicated that ozone may also deactivate the catalyst, causing a decrease in its activity, pointed to be due to the insertion of defects on the g- C_3N_4 structure and oxygenated groups at its surface.

The benefits of g- C_3N_4 have also been explored for disinfection proposes in recent years. Liu et al. [30] achieved a 4.80 and 4.24 log reduction of *E. coli* and *Staphylococcus aureus*, respectively, using ultrathin urea-based g- C_3N_4 with nitrogen vacancies under visible light, which kept its disinfection efficiency even after five runs. The presence of nitrogen vacancies coupled with a higher specific surface area was shown to be determinant of the catalyst's

bactericidal activity. Bacteriophage MS2 virus (*Emesvirus zinderi*) elimination using g-C₃N₄ was assessed by Li et al. [31], achieving a nearly 8-log reduction of the pathogen under 360 min. The photogenerated electrons and superoxide radicals were indicated as the main ones responsible for the virus inactivation, through the oxidation of their proteins.

Tungsten trioxide (WO₃) is a transition metal oxide that also appears as a promising photocatalyst to be used in chemical and biological CECs removal. The high photostability, corrosion resistance, low-cost fabrication, and bandgap of 2.5–2.8 eV are some of its benefits for photocatalytic usage [26]. Bulk WO₃ possesses a cubic perovskite structure and may be obtained in multiple crystalline forms, such as cubic, hexagonal, and monoclinic, the last being more stable at room conditions, formed between 17 °C and 330 °C.

The synthesis methods and procedures are determinants of the type of structure and the characteristics of the catalyst. The morphology and phases of WO₃ are especially relevant as it possesses multiple possible structures, affected by the synthesis method or post-treatments. Nagy et al. [32] found a direct influence of the pH of the solution during catalyst production on its obtained morphology, with a lower pH resulting in a cuboid shape (0.10), changing into nanorod (0.51), nanoneedles (1.52), and nanowires (2.01) with the respective increase of this parameter. Crystallinity may also be intentionally altered, resulting in different single or mixed phases, which present variations in the final product performance. Besides the pH, the addition of some compounds can alter WO₃ structures, such as polyethylene glycol and citric acid (Figure 2) [33]. This easy customization of the structure characteristics is a key advantage of WO₃, and their balanced effect can considerably increase the catalyst photoactivity for targeted applications.

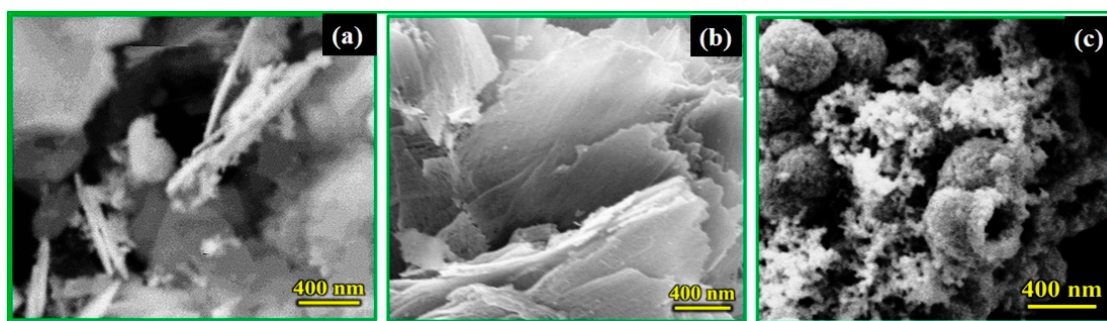


Figure 2. SEM images of WO₃ morphology alteration by variation of citric acid addition, (a) nanoflakes, (b) nanosheets, and (c) hollow spheres (Retrieved with permission from Ref. [33] Copyright (2020) Elsevier).

Different forms of WO₃ catalysts, synthesized through sol-gel and hydrothermal methods, have also been applied for photocatalytic ozonation by Mena et al. [34] for N,N-diethyl-meta-toluamide (DEET) abatement under visible light. Sol-gel monoclinic WO₃ calcinated at higher temperatures (600–700 °C) presented faster removals, eliminating DEET in 10 min. In comparison, over 2 h, the photocatalytic oxidation of DEET achieved only a 22% removal. The presence of ozone in the reaction medium can significantly decrease the typical high recombination rate of the photogenerated species.

The tungsten trioxide catalyst has also been tested for the treatment of more complex effluents. Razali et al. [35] used a WO₃ catalyst synthesized through the coprecipitation method, for the color and suspended solid removal of palm oil mill effluent (POME), retrieved from different ponds of the conventional treatment. The applied catalyst was able to obtain up to 65% and 91% color and suspended solids removal, respectively. The number of active surface sites and their adsorptive characteristics are appointed to be determinants over the treatment process.

Even with a higher visible-light photoactivity, the alternative catalysts still face compromising drawbacks for their application in more rounded contaminant treatment technologies. The lower specific surface areas, high electron-hole recombination, the limited

number of active sites, and low electron reduction potential are some examples of those disadvantages that still need to be circumvented [26].

Among different modifications, catalyst doping, and the production of different composites based on the commented catalysts appear as practical techniques to overcome these disadvantages. In the following sections, a recent overview of the general aspect of studies regarding the application of doped TiO₂ and composites of TiO₂ and the alternative catalysts for the photocatalytic degradation of contaminants will be given.

3. Catalyst Doping

3.1. TiO₂

TiO₂ is the most used semiconductor catalyst for the photocatalytic elimination of contaminants, but still presents some typical characteristics that hinder the process scale-up. Its high bandgap energy typically implies the use of external UV radiation sources, with $\lambda \leq 390$ nm, hampering its activation through sunlight as the UV portion represents only 4–6% [14]. The high recombination rate of e^-/h^+ and a weak separation of photocarriers also reduces its photocatalytic activity [25]. Among different modifications, catalyst doping thus appears as a practical technique to overcome these disadvantages. In this section, an overview of the general aspect of recent studies regarding the application of doped TiO₂ for the photocatalytic degradation of contaminants will be presented.

3.1.1. Transition Metals Doping

Both metal and non-metal elements may be incorporated in the catalyst structure and are capable of altering light absorption capacity and, more importantly, visible light, preventing the recombination of electron-hole [36]. Regarding metal doping, transition metals are more commonly applied, due to their partially filled *d* states, which promote the creation of intra-bandgap energy states and the absorption shift [37]. Table 1 summarizes the results and main conditions of the application of metal-doped TiO₂ found in the literature.

In reference to the catalyst synthesis, the sol-gel method is one of the main alternatives and allows better control of the product characteristics, such as porosity, structure, composition, and homogeneity, which is especially important in the incorporation of dopants. Moreover, a calcination step post-synthesis is usually applied as a simple technique to transform an amorphous structure into a crystalline (Anatase, Rutile, and Brookite). Karuppasamy et al. [38] attested that, during the investigation of the doping effect of different transition metals (Zn, Cu, and Zr) on TiO₂, the presence of doping elements may also alter the crystalline phase formation, reducing the temperature at the calcination stage needed to achieve the different structures, which was confirmed by other studies [39,40]. Regarding the different elements used and their photocatalytic activity, Zn-TiO₂ presented the best performance in methylene blue elimination under visible light. The interactions between Zn correspondent electronic states with the TiO₂ conduction band may provoke a red shift in the bandgap, improving the material light absorption between 400 nm and 700 nm.

The amount of dopant is also a crucial parameter to be studied, as excess material can lead to the formation of metallic oxides on the catalyst surface during thermal treatment, which may hinder the catalyst's exposure to photon irradiation. Lee et al. [39] applied hollow TiO₂ spheres doped with copper for the degradation of phenol under visible irradiation. To remove the copper oxides (CuO and Cu₂O), as detected in XRD and TEM analysis, an acid treatment was applied, capable of dissolving these species. The untreated catalyst presented minimal photodegradation, even lower than bare TiO₂, while acid-treated Cu-TiO₂ completely removed the contaminant in 4 h.

Table 1. Application of metal-doped TiO₂ for the photocatalytic removal of contaminants.

Catalyst	Precursor		Method	E _{bg} (eV)	Radiation Source	Contaminant	Removal (Time)	Ref.
	Ti	Dopant						
Ag-TiO ₂	-	Silver Nitrate	Precipitation	3.65	UV	Rhodamine B, 5 mg L ⁻¹	97% (20 min)	[41]
	-	Silver Nitrate	Ion-exchange	-	UV-Visible	Methyl Orange, 1 mg L ⁻¹	80% (150 min)	[42]
						<i>S. aureus</i> , 10 ⁶ CFU mL ⁻¹	100% (2 h)	
						<i>E. coli</i> , 10 ⁶ CFU mL ⁻¹	100% (1 h)	
Au-TiO ₂	TBOT	Gold (III) Chloride	Solvothermal	3.70	UV-Visible	Methylene Blue and Diuron, 0.03 mM each	65% MB (180 min) and 95% DIU (120 min)	[43]
Ce-TiO ₂	-	Cerium Nitrate	EDTA-Citrate	2.50	Solar	Ciprofloxacin and Norfloxacin, 10 mg L ⁻¹ each	93.2% CPR and 93.6% NOR (180 min)	[44]
						<i>E. coli</i> , 10 ⁸ CFU mL ⁻¹	95.0% (180 min)	
Cu-TiO ₂	TTIP	Copper Nitrate	Sol-gel	3.70	Visible	Methylene Blue, 0.05 M	27.5% (60 min)	[38]
	TBOT	Copper Nitrate	Sol-gel and Ion-exchange	2.38	Visible	Phenol, 5 mg L ⁻¹	100% (4 h)	[39]
Eu-TiO ₂	TTIP	Europium Oxide	Sol-gel	2.86	Visible	Methylene Blue and Methyl Orange, 5 mg L ⁻¹	72.1% MB and 71.8% MO (180 min)	[45]
Fe-TiO ₂	TTIP	Iron Acetylacetonate	Sol-gel	2.80	Visible	Acid Orange Azo Dye, 10 mg L ⁻¹	80% (60 min)	[46]
	TEOT	Iron Nitrate	Sol-gel	-	UV-Visible	Nitrobenzene, 2.45 × 10 ⁻⁴ M	97.3% (240 min)	[47]
La-TiO ₂	TTIP	Lanthanum Nitrate	Electrospinning	2.68	Visible	Ciprofloxacin and Methylene Blue, 10 mg L ⁻¹ each	91% MB and 99.5% CIP (300 min)	[48]
Mn-TiO ₂	TTIP	Manganese Acetate	Microwave-assisted Hydrothermal	1.65	UV	Prozac®, 10 mg L ⁻¹	95% (30 min)	[40]
Pr-TiO ₂	TTIP	Praseodymium Nitrate	Sol-gel	3.00	Visible	Acid Orange Azo Dye, 10 mg L ⁻¹	53% (60 min)	[46]
Zn-TiO ₂	TTIP	Zinc Nitrate	Sol-gel	2.83	Visible	Methylene Blue, 0.05 M	99.6 (60 min)	[38]
Zr-TiO ₂	TTIP	Zirconium Nitrate	Sol-gel	3.30	Visible	Methylene Blue, 0.05 M	81.9% (60 min)	[38]

Various factors are determinants of the performance and characteristics of doped catalysts, but regarding the element's properties, both the ionic radius and electronegativity are very important, due to their role over the element's solubility in TiO₂ lattice [49]. If the radius and electronegativity of the metal ion are close to Ti⁴⁺, doping tends to be substitutional, meaning that the substitution of the existing Ti⁴⁺ ions for the dopant will occur, but if the ion radius is lower than the existing elements, interstitial doping may occur, as they will occupy the interstitial sites of the catalyst lattice. Moreover, if the radius of the doping element is higher, it will not be able to penetrate the catalyst structure and will be mostly present at its surface [50].

Different analytical techniques may be applied to better detect the possible doping types. Through the study of a Mn-TiO₂ catalyst, Moreira et al. [40] detected a negative shift of the typical 144 cm⁻¹ E_g mode of anatase TiO₂ in Raman spectroscopy results, up to 5 cm⁻¹ with the increase of Mn%. This mode is representative of the symmetrical stretching of O-Ti-O bonds, and the presented shift was suggested to be indicative of the Mn³⁺ substitution of Ti⁴⁺. Moreover, Lee et al. [39] conducted an XPS analysis of Cu-TiO₂, and the results indicated a peak shift of the binding energy in both O 1s and Ti 2p spectrums, which was associated with the incorporation of Cu over the TiO₂ lattice, through substitution of Ti⁴⁺ by Cu²⁺ atoms, forming Cu-O-Ti bonds, also corroborated by

Cu 2p spectra, resulting in the modification of the electron density and charge distribution. Regarding interstitial and surface doping, Kayani et al. [51] studied vanadium doping TiO₂ and suggested that, in the XRD analysis, the reduction in the intensity of the anatase phase diffraction peak (101) is an indication of the interstitial doping of vanadium, which was expected due to the lower ionic radius of V⁵⁺ in comparison to Ti⁴⁺.

The efficiency of photocatalytic systems may also be improved by combination with other AOPs, such as ozonation, where the incorporation of ozone can increase radicals' formation and minimize photocatalytic drawbacks [52]. Ozone, as an excellent electron acceptor, can diminish electron-hole recombination by adsorbing onto the catalyst and retrieving the formed electrons, producing the ozonide radical ($\cdot\text{O}_3^-$) and engaging in multiple reactions, including the formation of hydroxyl and other radicals (Equations (1)–(3)).



Considering that one of the main advantages of catalyst doping is the reduction of E_{bg} and the resultant easier activation, their use in photocatalytic ozonation induces a higher electronic excitation, and thus an even higher radical generation. The ozone present in the medium may also directly react with the contaminants, especially those with high electron density, such as aromatic chemicals [53].

Catalyst doping is also an approach to turn photocatalytic ozonation into a more feasible technology by not only improving ozone decomposition but compensating the ozone production cost by using solar irradiation. Mecha et al. [54] demonstrated that, when applied for the photocatalytic ozonation treatment of phenol in SWW, Cu-TiO₂, Fe-TiO₂, and Ag-TiO₂ had an up to almost 40% lower energy requirement compared to the undoped catalyst, due to their increased activity. Moreover, notably, Fe-TiO₂ also maintained an appreciable activity under UV irradiation, indicating a broader active spectrum. Still, photocatalytic ozonation is not very much studied for the doped and codoped TiO₂ catalysts and there is plenty of space for developing this interesting and efficient technology. Moreover, the possibility of sunlight radiation usage, which is a natural resource available for a great part of the year, in such an approach is considered.

3.1.2. Noble and Rare-Earth Metals Doping

Noble metals (e.g., Au, Ag, Pd, Pt) represent a high-interest group of transition metals currently being vastly explored for TiO₂ doping due to their light-gathering capability and their role as electron trappers. These metals present, in general, a larger ionic radius compared to Ti⁴⁺, which difficult their penetration into the catalyst lattice, being deposited mostly on the surface. Saber et al. [43] detected multiple peaks corresponding to the presence of an Au crystalline phase in Au-TiO₂, prepared by solvothermal method, that can be indicative of surface modifications. Additionally, visible light absorption was considerably increased, again attributed to surface plasmon resonance.

Noble metal doping is known to produce a surface plasmon resonance effect, which induces a higher photoactivity of the catalyst under visible irradiation. This effect can be identified through diffuse reflectance spectroscopy (UV-Vis DRS), with a broader shoulder-like peak attributed to the heteroatom addition and the resulting oscillation of the conduction band electrons on its surface during photoirradiation [41]. Moreover, Ellouzi et al. [41] identified such a phenomenon, which resulted in considerable faster degradation of RhB, with an observed rate constant of 0.1827 min⁻¹ using a Ag-TiO₂ catalyst, while non-doped TiO₂ led to an apparent constant rate of 0.1034 min⁻¹. The lack of general and more specific legislation and regulation challenges the classification of CECs, but different synthetic dyes are also considered by many researchers as examples of CECs, due to their potential toxicity, with some studies already appointing their carcinogenic and mutagenic characteristics and ubiquitous behavior [55].

The use of noble metals in catalyst doping, especially silver, is also known to potentialize the antimicrobial activity of catalysts for disinfection purposes. In the medium, the metal particles present on the surface or even some that are released from the catalyst may interact with the cell membrane of microorganisms, damaging it and causing it to rupture, with the consequent oxidization of its proteins and genetic material (Figure 3) [42].

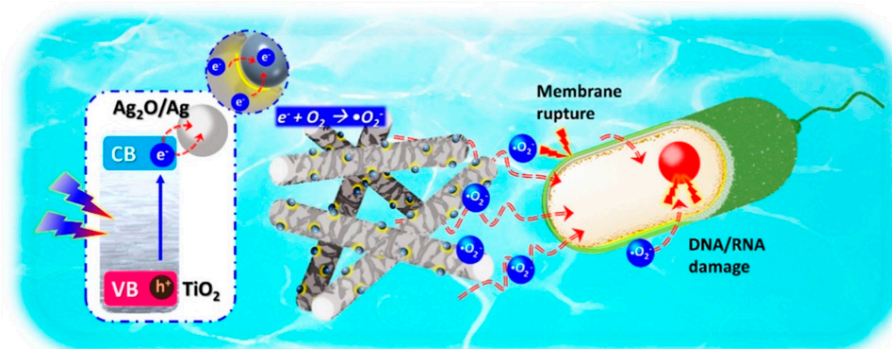


Figure 3. The mechanism for bacterial disinfection using Ag-TiO₂ (Retrieved with permission from Ref. [42] Copyright (2019) Elsevier).

Wu et al. [42] proved the capacity of Ag-TiO₂ nanofibers to inactivate *S. aureus* and *E. coli* bacteria. In 1 h, the number of bacterial colonies, initially $\sim 10^6$ CFU mL⁻¹, was substantially reduced when in contact with Ag-TiO₂ under visible light and eliminated in the next hour, while no significant inactivation was found for the undoped catalyst. A synergic effect between Ag₂O, AgO, and metallic silver, present in the catalyst surface, and the photogenerated radical species can considerably boost the disinfection capacity of the material, as it is able to rupture the bacteria cell membranes and degenerate their genetic material.

The surface plasmon resonance phenomenon and other positive effects of noble metals can also be an important ally in photocatalytic ozonation. However, specific properties of each element can greatly affect the final product performance and need to be evaluated for a better selection. For instance, the high electronegativity of Au (2.54) entails a higher capacity to withhold the photogenerated electrons. Although it could contribute to the mitigation of electron-hole recombination, it also impedes ozone reduction and ozonide radical formation, reducing the overall efficiency of the ozone-based process [56]. Thus, other elements with lower electronegativities can produce a more balanced effect, such as Ag (1.93), and boost contaminants removal while decreasing ozone consumption.

Rare-earth metals (e.g., Eu, Ce, Pr) also possess a high capacity to enhance the solar (visible and NIR) photocatalytic activity of TiO₂, in addition to its UV activity [23]. These elements are particularly interesting due to the partially filled 4f states, and the f-f electronic transitions present within. These electronic features combined with the interactions between the f and other orbitals, and with the TiO₂ CB and VB are responsible for the formation of new electronic states and other beneficial doping effects regarding luminescence properties [50]. The 5s and 5p orbitals also promote a shielding effect of the 4f orbital, producing a narrowing of the transition emission bands [57]. As their ionic radius is overall larger than Ti⁴⁺, the surface doping and formation of their respective oxide layers are expected, but multiple doping forms may occur simultaneously [57].

These metals can also considerably increase the number of defects over the catalyst surface, which may act as photogenerated species trapping sites. Moreover, even though, due to their ionic radius and symmetric difference, the impregnation of such elements occurs typically on the material surface, some studies have detected their presence within the catalyst structure [58].

The rare-earth metal doping can also influence the crystalline phase transition of TiO₂, which is known to inhibit the transition to rutile from the anatase phase, which possesses a higher photoactivity [58]. More specifically, Pascariu et al. [48] detected an

increase from 13% to 70% in the contribution of the anatase phase as a result of La^{3+} doping (Figure 4). Additionally, due to the crystalline phase composition, a higher number of surface defects, and OH groups when La^{3+} was applied, the doped catalyst performed a higher degradation of contaminants, ciprofloxacin, and methylene blue, under visible light. An optimum concentration of dopant was also found, with a further increase of lanthanum concentration higher than 0.1% possibly leading to the blocking of active sites and an excess of trap sites, with a shorter distance between them, having a controversial result, increasing electron-hole recombination [59,60].

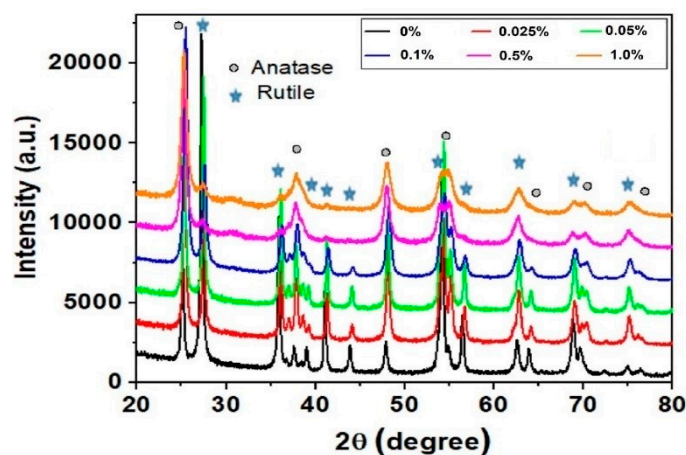


Figure 4. Crystalline phase transformation through La^{3+} at different concentrations (0–1.0%) (Retrieved with permission from Ref. [48] Copyright (2022) Elsevier).

Overall, noble and rare-earth metals are able to produce significant alterations in the catalyst light absorption characteristics and its charge separation. However, in a more practical application, other circumstances must be considered which may hinder their use. These elements possess typically high price precursors and, even if used in low concentration, in comparison to other earth-abundant materials, will elevate the material and consequently the final process cost, which is counter to what is needed to broaden the photocatalysis application. Moreover, they present intricate or distinct impregnations, necessitating a case-by-case analysis of their introduction to evaluate whether it will in fact produce the desired effect in more specific materials and morphologies. The high heterogeneity of studies involving such elements, with different impregnations, irradiation sources, contrasting results, and other parameters, challenge a proper selection of a more promising element.

3.1.3. Non-Metals Doping

Non-metal elements (e.g., N, S, B, C) are vastly explored for TiO_2 doping, with facile production methods, and capable of enhancing the catalyst stability and photoactivity, forming new energy levels with the consequent bandgap shortening, and inducing the formation of oxygen vacancies [37]. Contrarily to metals, in non-metal doping, it is expected that the introduced elements will have an influence over the valence band through interactions with O 2p states, even though cationic interactions may also take place [25]. Table 2 summarizes the application of different non-metals in TiO_2 doping.

Nitrogen doping is one of the most explored techniques, due to its promising red shift of the absorption edge and a similar ionic radius to oxygen, facilitating its substitution, although it may be inserted in the catalyst structure in different forms (Figure 5) [61]. Because of the broad exploration, different preparation methods have been applied, such as pulsed laser deposition [62], thermal annealing [63], hydrothermal [64,65], solvothermal [66], and sol-gel [67–69].

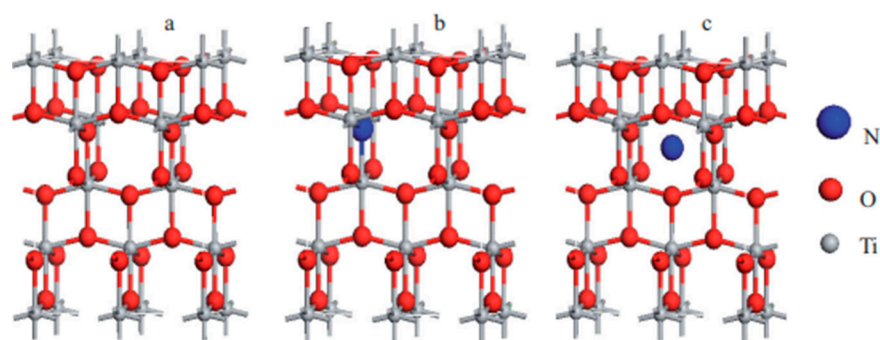


Figure 5. Schematics of different nitrogen incorporation over TiO_2 lattice: (a) pure TiO_2 , (b) substitutional, and (c) interstitial doping (Retrieved with permission from Ref. [70] Copyright (2009) John Wiley and Sons).

The sol-gel method is the most widely applied, due to its facile, flexible, and controllable operation, allowing different modifications of the basic processes to achieve the desired characteristics [50]. Using such a method, Assayehegn et al. [71] synthesized multiple N- TiO_2 catalysts applying different ratios of guanidium chloride (GUA), an environmentally friendly N precursor, to Ti, and indicated that the incorporation of N precursor showed a direct effect over the crystalline phase of N- TiO_2 formation post calcination. This can be caused by the perturbation of N^{3-} ions on the lattice orientation and density of charges, due to its higher negative charges and ionic radius compared to O^{2-} . Moreover, the found optimum mixed crystalline phase, 42% anatase and 58% rutile, is pointed out to have a beneficial synergic effect with nitrogen doping, which was also concluded by other research groups [39,68]. When applied for MB degradation under visible light, the best N- TiO_2 had an apparent reaction rate constant of 0.0325 min^{-1} , which is almost 17 times higher than the undoped catalyst, and represented 97% of MB removal within 100 min.

Dopant precursor is a key parameter, especially due to the large variety of compounds to be used. Bakre et al. [68] used semicarbazide, *N,N'*-dimethyl urea, and urea as nitrogen precursors in the sol-gel synthesis of N- TiO_2 . Regarding the crystalline phase composition, urea led to a pure anatase phase catalyst, while the other dopants resulted in rutile-anatase mixed phases. Following the characterization of the N- TiO_2 catalysts, the urea catalyst presented a higher absorption on the visible range, seconded by *N,N'*-dimethyl urea. FTIR spectroscopy results showed proper nitrogen incorporation over all catalysts lattice due to an indication of N-Ti-N bonds existence, possibly interstitially as suggested by N1s XPS spectra binding energies peaks. Additionally, other substances containing nitrogen have been vastly applied for doping, such as ammonia, ammonium hydroxide, ethylenediamine, and hydrazine hydrate [66,72–74].

Table 2. Application of non-metal doped TiO_2 for photocatalytic removal of contaminants.

Catalyst	Precursor		Method	E_{bg} (eV)	Radiation Source	Contaminant	Removal (Time)	Ref.
	Ti	Dopant						
B- TiO_2	* P25	Boric Acid	EDTA-Citrate	2.87	Solar	Ciprofloxacin and Norfloxacin, 10 mg L^{-1}	93.2% CPR and 93.0% NOR (180 min)	[44]
	TBOT	Boric Acid	Sol-gel	3.01	Visible	<i>E. coli</i> , 10^8 CFU mL^{-1}	99.9% (180 min)	
	TTIP	Boric Acid	Sol-gel	2.98	UV	Catechol, 10 mg L^{-1}	100% (60 min)	[75]
F- TiO_2	TiCl_4	Ammonium Fluoride	Nebulizer Spray	2.79	Visible	Diclofenac, 50 mg L^{-1}	98% (180 min)	[67]
I- TiO_2	TiCl_4	Ammonium Fluoride	Nebulizer Spray	2.79	Visible	Malachite Green, 300 mg L^{-1}	90% (60 min)	[76]
I- TiO_2	TBOT	Iodic Acid	Sol-gel	3.18	Solar	Methylene Blue, 4.8 mg L^{-1}	30% (60 min)	[77]

Table 2. Cont.

Catalyst	Precursor		Method	E _{bg} (eV)	Radiation Source	Contaminant	Removal (Time)	Ref.
	Ti	Dopant						
N-TiO ₂	TTIP	Urea	Sol-gel	2.27	UV	Diclofenac, 50 mg L ⁻¹	95% (180 min)	[67]
	TBOT	Guanidinium Chloride	Sol-gel	2.91	Visible	Methylene Blue, 10 mg L ⁻¹	97% (100 min)	[71]
	TTIP	Urea	Sol-gel	-			99% (100 min)	
	TTIP	N,N'-dimethyl urea	Sol-gel	-	Solar	Methylene Blue, 10 mg L ⁻¹	98% (120 min)	[68]
	TTIP	Semicarbazide	Sol-gel	-			98% (80 min)	
	TBOT	Urea	Sol-gel	2.58	Visible	<i>Microcystis aeruginosa</i> , 3 × 10 ⁶ cells mL ⁻¹	99.1% (12 h)	[78]
						<i>E. coli</i> , 10 ⁵ CFU mL ⁻¹	~100% (12 h)	
						<i>S. aureus</i> , 10 ⁵ CFU mL ⁻¹	~100% (12 h)	
	TTIP	Ammonium Hydroxide	Sol-gel	2.31	Visible	<i>Mycobacterium avium</i> , 10 ⁵ CFU mL ⁻¹	~100% (12 h)	[79]
						<i>Candida albicans</i> , 10 ⁵ CFU mL ⁻¹	99.9% (12 h)	
S-TiO ₂	TTIP	Sulfuric Acid	Flame Spray Pyrolysis	2.78	Visible	Acetaldehyde, 0.5 mM	65% (300 min)	[80]
	TTIP	Hydrogen Sulfide	Chemical Vapor Deposition	-	Visible	Methyl Orange, 5 mg L ⁻¹	38% (300 min)	[81]

* Commercial Degussa P25 TiO₂.

Sulfur emerges as an interesting dopant, presenting in both cationic and anionic species, as in the form of S⁶⁺ and S⁴⁺ it can substitute Ti⁴⁺, although the O²⁻ substitution by S²⁻ can also occur. Through the study of sulfur-doped TiO₂ films, Bento et al. [81] suggested that the cationic substitution by S⁶⁺ would be more advantageous for photocatalytic purposes in comparison to the anionic, due to the formation of impurity energy levels located above the TiO₂ valence band, decreasing the E_{bg} and improving activation by visible light. Furthermore, the authors verified the formation of SO₄²⁻ on the surface of the catalyst, known to occur during S doping, which may act as electron trap centers and improve radicals' formation. The replacement of O²⁻ by S²⁻ is may be less chemically favorable due to the larger ionic radius of the sulfur anion, hampering its penetration into the catalyst lattice and inducing higher thermodynamic energy for the S-Ti-S bond to be formed [80].

Boron has been found to promote a higher reduction of Ti⁴⁺ into Ti³⁺, which induces the formation of oxygen vacancies, a broader catalyst spectrum response, and improved photocatalytic activity. Yadav et al. [67] identified Ti³⁺ correspondent peaks in interstitially boron-doped TiO₂ Ti2p_{2/3} XPS spectra, indicating its existence in the catalyst lattice. Moreover, the full-width half maxima (FWHM) was used as a correlation of the presence of Ti³⁺, and when compared to a N-TiO₂ catalyst, it was found that B-TiO₂ presented a higher density of Ti at a less oxidized state. In addition, both N-TiO₂ and B-TiO₂ were compared regarding diclofenac degradation, and B-TiO₂ presented a higher photocatalytic activity, with an apparent constant rate value 30% higher than N-TiO₂. Zhang et al. [75] also confirmed the benefits of boron doping regarding Ti⁴⁺ reduction and suggested that, besides its role as electron trapping sites, Ti³⁺ altered the adsorptive properties of the catalyst. The formed O-Ti³⁺ bonds may weaken the water adsorption and enhance the formation of cooperative hydrogen bonds on the catalyst surface, promoting a higher interaction with contaminants, such as phenolic compounds.

Halogens, such as chlorine, iodine, and fluorine, possess attractive properties, such as high electronegativity and the capacity to occupy both titanium and oxygen sites [82]. Ravidhas et al. [76] successfully synthesized F-TiO₂ thin films and suggested that fluorine, the most electronegative element, could substitute oxygen atoms in the catalyst structure, leading to the formation of Ti-F-Ti bonds and the reduction of Ti⁴⁺, promoting an adjustment of the electron density of titanium and an increased concentration of oxygen vacancies.

This incorporation of impurities into the structure also caused a decrease of the E_{bg} down to 2.90 eV, from an initial 3.30 eV of the undoped catalyst. F-TiO₂ also presented an improved degradation of malachite green dye under visible and solar radiation, attributed to its higher surface area and number of active sites, oxygen vacancies, and lower E_{bg} . The disturbance of charges was also found by Hwang et al. [77] after iodine doping of TiO₂. In the I 3d XPS spectra, multiple valence states were found, with peaks corresponding to I⁵⁺, I⁷⁺, and I⁻ being detected in coexistence. The authors pointed out that I⁵⁺ had substituted Ti⁴⁺ atoms, due to their similar radius, with the ensuing formation of Ti³⁺ and Ti²⁺ due to compensation for the disproportionate charges. Meanwhile, the larger ionic radius of I⁻ induces its dispersion on the TiO₂ surface.

Apart from chemical contaminants, photocatalytic processes using non-metal doped catalysts have been applied for microorganisms' elimination, as a facile disinfection method that does not produce secondary pollutants [83]. The disinfection of a series of pathogenic contaminants, *S. aureus*, *E. coli*, *Mycobacterium avium*, and *Candida albicans*, was studied by Tzeng et al. [79] using a N-TiO₂ catalyst under visible light. Starting with a 10⁵ CFU mL⁻¹ individual solutions of each species, in 12 h treatment, N-TiO₂ obtained a final survival rate, C/C₀, of approximately 10⁻¹, 10⁻², 10⁻⁴ and 10⁻⁵ of, respectively, *C. albicans*, *M. avium*, *E. coli*, and *S. aureus*. The order of the disinfection yields is directly related to the complexity of the cells, as *C. albicans* is a unicellular fungus, it presents a higher structural complexity and contains substances less prominent to oxidative radicals' attacks, whereas *S. aureus* is a Gram-positive bacteria, which has no lipopolysaccharide layer.

The precursors may also deeply affect the disinfection characteristics of the material. Using urea and N₂ as nitrogen precursors, Zhou et al. [78] demonstrated that even with the catalyst only calcinated in the presence of N₂ having the highest incorporation of nitrogen, the urea doped catalyst calcinated in the same atmosphere presented a removal of 99% of chlorophyll-a, related to the *Microcystis aeruginosa* algae cells degradation, in 12 h.

The doping process may also lead to the formation of other compounds within the catalyst structure, such as the elements' respective oxides, which may provide additional mechanisms for chemical and biological contaminant removal. For instance, regarding boron doping, the formation of a B₂O₃ can enhance the catalyst bacterial inactivation ability, as it can dissolve in water and lead to the formation of boric acid [44,84].

The typical low cost of non-metal precursors can be an interesting aspect to reduce photocatalytic ozonation costs. As said previously, the combined process may present an increased cost due to ozone production energy requirement and possible use of artificial radiation sources, in the case of typical TiO₂. Thus, the lower cost associated with non-metal doping and the produced benefits, such as the increase in photocatalytic activity under solar radiation, may render the photocatalytic ozonation process more feasible. In previous studies, Fernandes et al. [18,21] developed multiple nitrogen-doped catalysts for application in the photocatalytic ozonation removal of a mixture of parabens. The doped catalyst, especially ammonia doped, led to an improved degradation of all five contaminants (methyl-, ethyl-, propyl-, butyl-, and benzylparaben), completely removing them faster and with a lower consumption of ozone. As ozone has low solubility in water, the photocatalyst may enhance its solubilization and decomposition, allowing a more efficient consumption, leading to a lower concentration needed through the production of other reactive species.

3.1.4. Co-Doping

The application of two or more dopants can be highly beneficial, as it can enhance the catalyst performance through multiple mechanisms. Multiple combinations of elements are possible and have been explored, even with different classifications, such as metal and non-metal co-doping. The co-doped Fe-Pr-TiO₂ catalyst, studied by Mancuso et al. [46], presented an improved performance regarding AO dye removal compared to the single and undoped catalyst, with 87% removal of the AO and 80% TOC removal in 60 min under visible light. In the studied case, the co-doping was accounted to considerably decrease the E_{bg} (2.7 eV) and enhance the formation of oxygen vacancies, confirmed in photolumi-

nescence spectra, acting as electron trappers, and reducing the e^-/h^+ recombination. The authors also investigated in another study the co-doping of Fe and N, and again it showed a superior performance as it can benefit from both the substitution of Ti^{4+} by Fe^{3+} , acting as electron acceptors and inhibiting e^-/h^+ recombination, and the nitrogen replacement of oxygen sites, producing Ti^{3+} and oxygen vacancies [59].

Jahdi et al. [85] explored the combination of fluorine with palladium for the degradation of sulfamethoxazole (SMX), using a hydrothermal-produced F-Pd-TiO₂ catalyst. The addition of F was suggested to control the crystalline phase growth, while Pd significantly improved the photocatalytic activity under higher wavelengths, with its increasing concentration (0–10%) leading to E_{bg} down to 0.54 eV. The best catalyst achieved 98.4% of SMX removal under direct sunlight in 40 min. It should be noticed though that the presence of fluorine was found to lead to the formation of white fluorine-based polymeric substances floating in the treated solution.

Different precursors may be used to incorporate more than one element simultaneously [86]. Thiourea is commonly used as a source of carbon, sulfur, and nitrogen, and the three dopants' simultaneous incorporation may promote an even more significant narrowing of the bandgap of TiO₂ through the formation of mid-gap levels due to interactions with the O 2p orbitals. Additionally, Khedr et al. [86] indicated that sulfate and carbonaceous species can also be formed and may improve the photocatalytic activity, acting as electron trapping sites, inducing visible-light absorption, and enhancing radicals' formation. In this specific study, N-C-S-TiO₂ had substantially better performance over ibuprofen degradation under visible light irradiation, almost fully eliminating the contaminant under 240 min of reaction, against a 12.2% degradation reached by the undoped catalyst. Table 3 presents some key studies involving the use of co-doped TiO₂ catalysts.

Table 3. Application of co-doped TiO₂ for photocatalytic removal of contaminants.

Catalyst	Precursor		Method	E_{bg} (eV)	Radiation Source	Contaminant	Removal (Time)	Ref.
	Ti	Dopant						
C-Co-TiO ₂	TTIP	Glucose and Cobalt Chloride	Co-precipitation	2.81	Visible	Phenol, 100 mg L ⁻¹	100% (120 min)	[87]
C-N-TiO ₂	TBOT	Extrapallial Fluid of Mussels	Chemical Deposition	2.90	Visible	High-density Polyethylene, 0.4% w/v	72.0% (50 h)	[88]
C-N-S-TiO ₂	Ti ₂ (SO ₄) ₃	Thiourea	Hydrothermal	2.90	Visible	Ibuprofen, 20 mg L ⁻¹	100% (5 h)	[86]
Cu-N-TiO ₂	TTIP	Urea and Copper (III) Nitrate	Sol-gel	-	Visible	Methylene Blue, 12.5 mg L ⁻¹	56.3% (90 min)	[89]
F-N-TiO ₂	TBOT	Ammonium Fluoride and 2-nitrophenol	Solvothermal	-	Solar	2-nitrophenol, 10 mg L ⁻¹	~98.1% (75 min)	[90]
		Ammonium Fluoride and 4-nitrophenol		-	Solar	4-nitrophenol, 10 mg L ⁻¹	~93.9% (75 min)	
F-Pd-TiO ₂	TBOT	Trifluoroacetic Acid and Palladium Chloride	Microwave-assisted Hydrothermal	0.54	Solar	Sulfamethoxazole, 30 mg L ⁻¹	98.4% (40 min)	[85]
Fe-Eu-TiO ₂	TTIP	Europium Oxide and Iron Nitrate	Sol-gel	2.78	Visible	Methylene Blue and Methyl Orange, 5 mg L ⁻¹	97.9% MB and 99.7% MO (180 min)	[45]
Fe-N-TiO ₂	TTIP	Urea and Iron Acetylacetonate	Sol-gel	2.70	Visible	Acid Orange Azo Dye, 10 mg L ⁻¹	90% (60 min)	[59]
Fe-Pr-TiO ₂	TTIP	Praseodymium Nitrate and Iron Acetylacetonate	Sol-gel	2.70	Visible	Acid Orange Azo Dye, 10 mg L ⁻¹	87% (60 min)	[46]

3.2. WO₃

The WO₃ photocatalysts appear as an interesting alternative to typical TiO₂, with good visible-light activity, but also chemical and electronic properties [91]. However, some drawbacks are still found, principally the high electron-hole recombination rate and a

more positive position of the CB, which compromises the superoxide production [50]. The introduction of heteroatoms to the WO_3 structure has not been widely explored compared with other catalysts, but some studies have been conducted showing that this adaptation may be responsible for promoting the enhancement of the catalyst performance and its typical disadvantages. Studies regarding the application of doped WO_3 catalysts are summarized in Table 4.

Table 4. Application of doped WO_3 for photocatalytic removal of contaminants.

Catalyst	Precursor		Method	E_{bg} (eV)	Radiation Source	Contaminant	Removal (Time)	Ref.
	W	Dopant						
Ag- WO_3	Sodium Tungstate	Silver Nitrate	Hydrothermal, HCl	2.63	Solar	Acetaminophen, 5 mg L ⁻¹	75.4% (120 min)	[92]
Cd- WO_3	-	Cadmium Nitrate	Ion-exchange	1.85	Visible	Methylene Blue, 10 mg L ⁻¹	75.5% (80 min)	[93]
Co- WO_3	Sodium Tungstate	Cobalt Chloride	Co-precipitation	-	Visible	Methyl Red, 10 mg L ⁻¹	90% (120 min)	[94]
Cu- WO_3	-	Copper Nitrate	Precipitation	2.60	Visible	Tetracycline, 50 mg L ⁻¹	96.7% (120 min)	[95]
Fe- WO_3	Ammonium Paratungstate	Iron Chloride	Sol-gel	2.39	Visible	Methylene Blue, 10 mg L ⁻¹	95% (120 min)	[96]
Gd- WO_3	Sodium Tungstate	Gadolinium Nitrate	Hydrothermal	2.64	Visible	Rhodamine B, 20 mg L ⁻¹	94% (100 min)	[97]
Mn- WO_3	Tungstic Acid	Manganese Chloride	Microwave-assisted Precipitation	2.00	Visible	Sulfamethoxazole, 1 mg L ⁻¹	100% (70 min)	[98]
C- WO_3	Sodium Tungstate	Carbonized Glucose	Hydrothermal	-	UV-Visible	Rhodamine B, 20 mg L ⁻¹	95% (180 min)	[99]
I- WO_3		Ammonium Iodide		2.17			88.2% TOC 89.1% COD (240 min)	
P- WO_3	Ammonium Paratungstate and <i>Spondias mombin</i> leaves extract	Ammonium Phosphate	Hydrolysis and Precipitation	2.41	Solar	Dyeing Wastewater, TOC = 576.8 mg L ⁻¹ COD = 991 mg L ⁻¹	86.8% TOC 86.6% COD (240 min)	[100]
P-I- WO_3		Ammonium Phosphate and Ammonium Iodide		2.02			93.4% TOC 95.1% COD (240 min)	
S- WO_3	Sodium Tungstate	Thiourea	Hydrothermal	-	Visible	Methyl Orange, 20 mg L ⁻¹	97% (3 h)	[101]

3.2.1. Transition Metals Doping

WO_3 doping can considerably interfere with basic catalyst characteristics, such as crystallinity, morphology, and optical properties, which will then produce variations in their photocatalytic activity. Cu- WO_3 was found to have a lower E_{bg} (2.78 to 2.60 eV) and higher crystallinity compared to the studied undoped catalyst by Quyen et al. [95]. Besides, changes in its surface properties were also detected, with the incorporation of Cu being mainly at this level, promoting the formation of a more porous structure, meaning a higher surface area and number of active sites capable of enhancing contaminants' interaction and degradation. The presence of the heteroatom also promoted a higher presence of the W^{5+} state, which may imply the equivalent formation of oxygen vacancies due to electronic rebalance, which may increase the catalyst electroconductivity and pollutants adsorption.

Mehmood et al. [94] also presented a broad study of the incorporation of another metallic element, cobalt, over the WO_3 lattice. The Co atoms were appointed to be doped substitutionally, by the replacement of W^{6+} by Co^{2+} , which promoted an expansion of the lattice due to the slightly higher ionic radius of Co^{2+} . Thus, excessive addition of the dopant could degrade the catalyst crystallinity due to the collapse of its structure. The dopant also supported the creation of localized states within the catalyst bandgap, reducing the E_{bg} . The Co- WO_3 presented incredibly better performance for the degradation of a methyl red solution, increasing the removal rate from less than 5% to 90% under 2 h. Additionally, the use of this catalyst was also applied for the inactivation of cancerous cells, which reduced

the viability of MCF-7 breast cancer and Hep-2 liver cancer cells down to 60%, possibly through the attack of their mitochondria and rupture of the cell wall.

The doped catalysts must also be subjected to lixiviation tests, especially when more dangerous metal elements are used, as their continuous reutilization may be responsible for the release of this species into the medium. The use of cadmium (Cd) as a metal dopant has been indicated to diminish e^-/h^+ pairs recombination and increase the catalyst crystallinity and porosity, resulting in a higher photocatalytic degradation [93]. However, although the dopant may substitute W atoms on the catalyst structure, implying stronger bounds, Cd lixiviation can still occur, especially at acidic conditions. It must be noted that US EPA regulations, for example, establish a maximum of 0.005 ppm of cadmium in drinking water, with serious negative health effects when in contact with higher concentrations.

3.2.2. Noble and Rare-Earth Metals Doping

The use of different precursors during the photocatalyst and doping synthesis can alter the mechanisms and the configuration of the formed product. Palharim et al. [92] studied the alteration caused by the addition of HCl or HNO₃ during Ag-WO₃ synthesis, using AgNO₃ as the dopant precursor. It was found that HNO₃ promoted the incorporation of the dopant metallic silver, while HCl reacted with AgNO₃ to form AgCl, being detected in the catalyst structure. This promoted differences in the catalyst, as an increase in Ag concentration led to lower E_{bg} in HNO₃/Ag-WO₃ due to the particle agglomeration, and the opposite occurred for HCl/Ag-WO₃. Regardless of the acid used, Ag-WO₃ had better removal rates of acetaminophen under visible light than the undoped catalyst, because of the combination of factors such as the localized surface plasmon resonance, characteristic of noble metal doping, the insertion of new energy level within the catalyst bandgap and the reduction of E_{bg} . Moreover, HCl doped presented a better performance, possibly due to the interaction between Ag-WO₃ and the AgCl clusters formed, and the contribution towards decreasing the WO₃ conduction band to more negative values, allowing oxygen reduction.

The f-orbitals of rare-earth metals can also be beneficial for the improvement of WO₃ performance. Tahir and Sagir [102] conducted a wide study of the application of these metals by synthesizing lanthanum-, erbium- and gadolinium-doped WO₃ through a hydrothermal method. As these rare-earth metals possess considerably higher ionic radius, the substitution of W atoms is not favored, and the dopants were found to occupy interstitial sites. The catalyst crystallite size decreased with the incorporation of the heteroatoms, having advantages regarding the reduction of photogenerated species recombination, and the specific surface areas were also greatly increased, especially for Gd-WO₃, 106 m² g⁻¹ compared to 30.7 m² g⁻¹ of the undoped catalyst. Moreover, the higher adsorption locations and catalytic center of Gd-WO₃, combined with lower recombination of electron-hole, presented a faster and almost complete removal of multiple single contaminants (methotrexate, tetracycline, methyl orange, methylene blue, and crystal violet).

3.2.3. Non-Metals Doping

The combination of the non-metal elements and WO₃ can also promote variations of the CB and VB of the catalyst, hinder the recombination factor of photoinduced charges, and increase photocatalytic activity under visible light. The S-WO₃ nanowires catalyst was investigated by Han et al. [101] using thiourea as the sulfur precursor. The non-metal element was able to substitute W⁶⁺ in the form of S⁶⁺ in the WO₃ lattice, as opposed to the anionic replacement of O²⁻, due to the higher energy form of W-S bonds than W-O. The doping method also accounted for the formation of surface hydroxyl groups because of oxygen adsorption, which may act as electron trapping centers. Sulfur also was responsible for creating intermediate energy levels above the VB of WO₃, enhancing the catalyst's photoresponse. Even if not mentioned by the authors, the use of thiourea as a precursor could also involve the parallel incorporation of nitrogen over the structure.

Similar effects were found regarding the positive effects of non-metallic heteroatoms by Zheng et al. [99], in interstitially carbon-doped WO₃. The location of the C atoms

may denote its interaction with WO_3 and consequent distortion of the WO_6 octahedron structure and an induced increased dipole, possibly more conducive for the transmission of photocarriers and photocatalytic activity. Comparably with other non-metals, new C 2p induced levels were formed in the interior of the bandgap of WO_3 , acting as transfer stations to the photocarriers.

3.2.4. Co-Doping

As dopants may have different mechanisms, their combination can severely upgrade the photocatalytic activity through the synergic combined effect, being able to attain higher removal rates, even at complex effluents. Tijani et al. [100] proposed a green synthesis of I-P- WO_3 , by applying a plant extract in bulk catalyst production. The I^- and P^{3+} atoms acted as structure-directing agents, affecting the morphology of the rod-like catalyst, with P conducting to more elongated shapes and I with shorter and more uniform. Alterations of lattice parameters indicated distortions of the catalyst structure, which may be a result of the partial substitution of W^{6+} and O^{2-} , by respectively P^{3+} , which has a smaller ionic radius than W, and I^- that has a higher ionic radius compared to O. This substitution is pointed out to have detrimental effects as it may occur the collapsing of the WO_3 structure. However, due to the low concentration of the incorporation, it only resulted in beneficial decreased grain sizes and enhanced surface areas, up to $416.3 \text{ m}^2 \text{ g}^{-1}$. The optical properties of I-P- WO_3 were also improved, decreasing the E_{bg} from 2.61 to 2.02 eV, due to acceptor energy levels below the CB of WO_3 . The codoped catalyst was applied for the treatment of dyeing wastewater under sunlight, achieving high color and odor removal, as well as 93.4%, 95.1%, and 92.0% removals of total organic carbon (TOC), chemical, and biological oxygen demand (COD and BOD), respectively, accounting for values below the regulated international standards. Thus, codoping may lead to the formation of a more feasible photocatalyst regarding more complex applications.

3.3. g- C_3N_4

Even with a typically lower E_{bg} compared to TiO_2 , g- C_3N_4 still exhibits a fast recombination rate of the photogenerated e^-/h^+ pairs and a limited light absorption range, which diminishes the visible and solar radiation conversion. Thus, the doping of g- C_3N_4 may contribute to charge separation and concurrently a shift of light absorption. As g- C_3N_4 has gotten much attention recently, investigation of the incorporation of multiple elements over the catalyst structure has been reported.

3.3.1. Metals Doping

The doping using metallic elements is known to promote the formation of oxygen vacancies and considerably improve the catalyst activity. The existence of various unbounded electrons in the hexazine structures of g- C_3N_4 makes it susceptible for metallic elements to be inserted in its lattice [103]. The results regarding the use of metal-doped g- C_3N_4 are present in Table 5. For the removal of paracetamol under visible light, doping using cobalt (II) nitrate was made over a melamine-based g- C_3N_4 through a calcination method [104]. The detected Co^{2+} and Co^{3+} in the catalyst and the O 1s XPS spectra indicated the formation of oxygen vacancies. Moreover, the doping affected the crystallinity of g- C_3N_4 and its morphology, presenting a mixed structure of cobalt oxide closely attached to carbon nitride layers. Optical characterization also showed indirect recombination of charge carriers and smaller charge transfer resistance, which indicates a higher charge transport kinetics and separation. Ultimately, the Co-doped g- C_3N_4 presented a reaction rate almost three times higher than the undoped catalyst, 0.0382 min^{-1} , completely removing 1 mg L^{-1} of paracetamol within 120 min. No leaching of Co ions was detected after the oxidation experiments.

Pham et al. [105] studied Ni-doped g- C_3N_4 for volatile organic compounds (VOCs), nitrobenzene, and toluene, removal under natural sunlight. The presence of Ni promoted a red shift of the absorption edge, suggesting a higher photoactivity over the visible range,

and E_{bg} was estimated as 2.25 eV, noticeably lower than the undoped $g\text{-C}_3\text{N}_4$, 2.76 eV. The doped catalyst also presented a higher specific surface area and pore volume, which promote a higher interaction with the different compounds involved in the oxidative reactions. The doping treatment finally improved VOCs elimination, with reaction rate constants of 0.0170 and 0.0173 min^{-1} for, respectively, toluene and nitrobenzene, compared with 0.0049 and 0.0072 min^{-1} of the undoped catalyst.

The incorporation of iron over $g\text{-C}_3\text{N}_4$ can also improve the oxidation potential and may act as electron trap centers. With a relatively larger ionic radius, Fe atoms tend to be doped into the interlayers of the catalyst, forming strong bonds with the N atoms present in the aromatic rings, which decreases the E_{bg} . However, an excess amount of Fe may also cause the collapse of the sheet structure. The dopant exists mainly as Fe^{3+} , and as the reduction potential of $\text{Fe}^{3+}/\text{Fe}^{2+}$ lies between the CB and VB of $g\text{-C}_3\text{N}_4$, the photogenerated e^- may easily react with Fe^{3+} , reducing it into Fe^{2+} and diminishing e^-/h^+ recombination. The instability of Fe^{2+} makes it prone to suffer oxygen reduction and return to the Fe^{3+} form [103].

Although not often, the use of alkaline and alkaline-earth metals (such as K, Mg, and Ca) for $g\text{-C}_3\text{N}_4$ doping has been explored. Studies regarding the use of these elements in more surveyed catalysts present mixed results, with possibly poisoning effects, but also an increase in photoactivity and surface area [50]. Tripathi and Narayanan [106] tested potassium doping of melamine-based $g\text{-C}_3\text{N}_4$. The presence of K during the thermal polymerization was suggested to inhibit the formation of hydrogen bonds between the polymeric melon strings of the intra-layer infrastructure, reducing the layer's stacking, but also the E_{bg} , from 2.7 to 2.5 eV, with changes of the VB energy and Fermi level towards more positive potentials. This condition may promote an increase in the oxidation capacity of the K-doped catalyst. Furthermore, under natural sunlight, the doped catalyst obtained 56.5% elimination of phenol present in real wastewater.

3.3.2. Noble and Rare-Earth Metals Doping

Noble metals, such as Ag and Au, are electron-rich transition metal elements that can capture photogenerated electrons and provide the excess energy of plasmonic states, provoking a shift of the Fermi levels to less positive potentials due to an excess of negative charges, reducing electron-hole recombination and boosting its catalytic performance. Tri et al. [107] explored Ag-doped $g\text{-C}_3\text{N}_4$ for the treatment of tetracycline, an antibiotic, in hospital wastewater under solar irradiation. Besides the faster production and higher separation of the e^-/h^+ , Ag significantly altered the optical properties of the catalyst, decreasing its E_{bg} down to 2.19 eV, and possibly increasing the number of active sites and surface area, culminating in an optimum removal of 96.8% of tetracycline under 120 min.

Bawazeer et al. [108] also proposed a facile ball mill-assisted synthesis method for Au-doped $g\text{-C}_3\text{N}_4$, without the use of solvents. Even with no significant modification of the E_{bg} and a decrease in specific surface area, the presence of gold atoms boosted the catalyst performance over Arsenazo III dye decolorization, eliminating the contaminant within 50 min and with a reaction rate constant 2.5 times higher. The role of Au as recombination centers and a higher charge photogeneration due to the surface plasmon resonance is appointed to be responsible for the improved efficiency.

Due to their unfilled f-orbitals, rare-earth metals may act as trapping sites, distributing the photogenerated carriers, but can also form complexes with Lewis bases by bonding with their respective functional groups, promoting a higher interaction with organic pollutants at the catalyst surface. An Er-doped $g\text{-C}_3\text{N}_4$ was produced by Li et al. [109], with the dopant existing in the Er^{3+} state. The foreign element promoted a higher degree of polymerization and crystallization of the $g\text{-C}_3\text{N}_4$ network, but when in excess may also weaken tri-s-triazine bonds. The doped catalyst showed great efficiencies towards the degradation of three different contaminants, i.e., RhB, tylosin, and tetracycline, under simulated solar irradiation, with kinetics rate constants, respectively, 3.6, 1.6, and 1.7 times higher than the bulk $g\text{-C}_3\text{N}_4$. Additionally, Er^{3+} presented a detrimental effect over the specific surface area,

which indicates that changes in the optoelectronic properties may play more important roles in the photodegradation performance.

Table 5. Application of metal-doped g-C₃N₄ for photocatalytic removal of contaminants.

Catalyst	Precursor		Method	E _{bg} (eV)	Radiation Source	Contaminant	Removal (Time)	Ref.
	C ₃ N ₄	Dopant						
Ag-g-C ₃ N ₄	Melamine and Urea	Silver Nitrate	Thermal Polymerization and Ion-exchange	2.19	Solar	Tetracycline, 20 mg L ⁻¹	96.8% (120 min)	[107]
	Melamine	Silver Nitrate	Thermal Polymerization	2.46	Visible	Oxytetracycline, 10 mg L ⁻¹ and Antibiotics Wastewater: Oxytetracycline, 101.5 mg L ⁻¹ ; Tetracycline, 85.3 mg L ⁻¹ ; Gatifloxacin, 89.4 mg L ⁻¹	98.6% (120 min) 94.5% OTC, 81.8% TC, 67.3% GFA (120 min)	[110]
Au-g-C ₃ N ₄	Melamine	Au NPs	Thermal Polymerization	2.86	Visible	Arsenazo, 4 mg L ⁻¹	100% (60 min)	[108]
Co-g-C ₃ N ₄	Melamine	Cobalt Nitrate	Thermal Polymerization	2.38	Visible	Paracetamol, 10 mg L ⁻¹	96.3% (120 min)	[104]
Er-g-C ₃ N ₄	Melamine	Europium Nitrate	Thermal Polymerization	2.50	Solar	Tetracycline, 25 mg L ⁻¹ Tylosin, 25 mg L ⁻¹	85% (90 min) 70% (90 min)	[109]
	Cyanuric Acid and Melamine	Europium Chloride	Thermal Polymerization	2.70	Visible	Rhodamine B, 10 µg L ⁻¹	90% (30 min) 100% (90 min)	[111]
Fe-g-C ₃ N ₄	Melamine	Iron Nitrate	Thermal Polymerization	2.73	Visible	Rhodamine B, 10 mg L ⁻¹	100% (150 min)	[103]
K-g-C ₃ N ₄	Melamine	Potassium Chloride	Thermal Polymerization and Ion-exchange	2.50	Solar	Phenolic Effluent, Ph = 980 mg L ⁻¹ and COD = 6300 mg L ⁻¹	56.5% (300 min)	[106]
	Thiourea	Potassium Bromide	Thermal Polymerization	2.15	Visible	Nitric Oxide, 600 ppb	36.8% (30 min)	[112]
Ni-g-C ₃ N ₄	Melamine	Nickel Nitrate	Thermal Polymerization	2.25	Solar	Toluene and Nitrobenzene, 5 mg L ⁻¹	85.8% TOL 98.6% NBZ (120 min)	[105]
V-g-C ₃ N ₄	Melamine	Ammonium Metavanadate	Thermal Polymerization	2.63	Solar	Tetracycline, 10 mg L ⁻¹	81.9% (240 min)	[113]

3.3.3. Non-Metals Doping

Non-metal and metalloid elements have a larger record of use in g-C₃N₄ doping and are able to overcome the disadvantageous surface characteristics of the catalyst and improve its electronic and optical properties. Table 6 presents the results of the use of non-metal doped g-C₃N₄.

Zhang et al. [114] synthesized a mesoporous g-C₃N₄ which presented a high specific surface area, 91.1 m² g⁻¹, due to its porous structure, providing a larger number of active sites. However, due to the quantum size effect, the UV-Vis absorption spectrum suffered a blue shift as bandwidth decreased with the concurrent decrease of particle size. It was found that oxygen doping, besides the reduction of the photo-induced carriers' recombination, may compensate for the absorption blue shift and enhance photocatalytic activity under simulated solar irradiation. The oxygen-doped mesoporous catalyst attained incredibly faster quasi-first-order kinetic constants for RhB and MO degradation, 64 and 24 times higher than simple mesoporous g-C₃N₄.

Significant surface alterations may also be found when doping with oxygen, as investigated by Praus et al. [115]. The authors presented a facile synthesis of the doped catalyst, by the combination of melamine and cyanuric acid, an oxygen-rich compound, in the thermal polymerization step. The modification increased the catalyst specific surface area from 14 to up to 41 m² g⁻¹ and a lowering of protonated nitrogen groups at the

catalyst surface occurred, by means of substitution by -OH and -O- groups. Under LED lights, the O-doped g-C₃N₄ presented faster kinetic rates regarding ofloxacin and RhB, i.e., ~30 mol L⁻¹ min⁻¹ and ~3 min⁻¹, respectively. The conduction and valence bands potentials at pH 7 were also calculated against normal hydrogen electrode (NHE), with the best doped catalyst presenting values of -0.93 and 1.69 eV, respectively. As the redox potential of hydroxyl radicals, E⁰(·OH/H₂O), is 2.74 eV, which means the oxidation of water to form commented radicals by the positive holes at the VB is not energetically favored, the direct contaminant oxidation by h⁺ and superoxide radicals are the main degradation mechanisms (Figure 6). An interesting approach to overcome the low production of ·OH due to the respective low VB potential would be the incorporation of ozone in the reaction. The ozonide racial redox potential, E⁰(·O₃⁻/O₃), is within the catalyst band potential, 0.89 eV, which can improve the production of radicals including •OH through consecutive reactions (Equations (1)–(3)) [116].

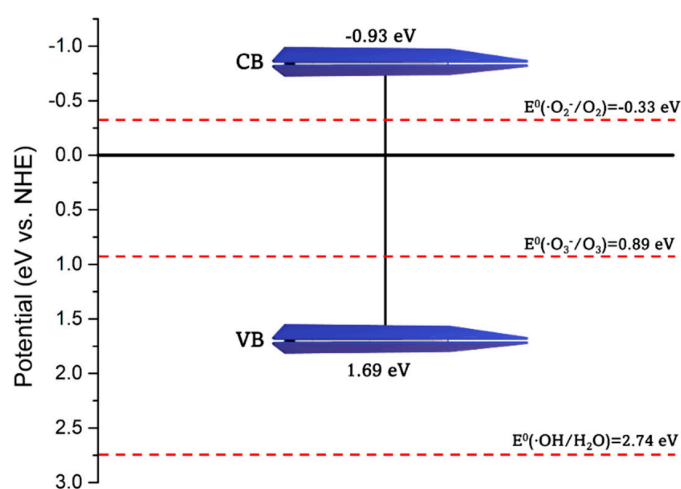


Figure 6. Representation of the energy diagram of Ag-g-C₃N₄ CB and VB potentials [115].

Other elements, such as silicon and phosphorous, have been indicated to substantially alter the bandgap energy and/or position of CB and VB of g-C₃N₄ catalysts, due to orbitals interaction. Wang et al. [117] produced P-doped g-C₃N₄ nanobelts and showed a significant decrease of the CB compared to bulk g-C₃N₄, -0.92 to -0.04 eV, with P successfully substituting C atoms, and even with a less negative CB, e⁻/h⁺ recombination was reduced and p-hydroxybenzoic acid degradation increased from 33.1% to 77.3%, by comparison of undoped and P-doped nanobelt catalysts. Once more, as the CB is less negative than E⁰(·O₂⁻/O₂), -0.33 eV, the superoxide may not be generated, and the presence of ozone would be beneficial as it possesses higher E⁰ and may act as the main electron acceptor.

Liang et al. [118] suggested that, when a silicon-doped catalyst was synthesized, N-Si bonds may act as electron trap centers, as it forms impurity levels close to the conduction band of g-C₃N₄, facilitating the interaction between e⁻ and respective acceptors, oxygen or ozone.

Table 6. Application of non-metal-doped g-C₃N₄ for photocatalytic removal of contaminants.

Catalyst	Precursor		Method	E _{bg} (eV)	Radiation Source	Contaminant	Removal (Time)	Ref.
	C ₃ N ₄	Dopant						
B-P-g-C ₃ N ₄	Melamine	Boric and Phosphoric Acid	Thermal Polymerization and Hydrothermal	2.66	Visible	Diclofenac, 10 mg L ⁻¹	100% (90 min)	[119]
Cl-g-C ₃ N ₄	Dicyandiamide	Cyanuric Chloride	Solvothermal	1.78	Visible	Rhodamine B, 10 mg L ⁻¹	99.6% (125 min)	[120]
	Melamine	Ammonium Chloride	Thermal Polymerization	2.71	Visible	Rhodamine B, 10 mg L ⁻¹	57.8% (30 min)	[121]

Table 6. Cont.

Catalyst	Precursor		Method	E_{bg} (eV)	Radiation Source	Contaminant	Removal (Time)	Ref.
	C_3N_4	Dopant						
O-g- C_3N_4		Semicarbazide Hydrochloride	Molten-salt	2.25	Visible	Naproxen, 100 mg L ⁻¹	100% (5 h)	[122]
	Urea	Hydrogen Peroxide	Thermal Polymerization and Solvothermal	2.94	Solar	Rhodamine B, 10 mg L ⁻¹ Methyl Orange, 10 mg L ⁻¹	95% (20 min) 70% (4 h)	[114]
	Urea	Cyanuric Acid	Thermal Polymerization	2.62	Visible	Rhodamine B, 10 mg L ⁻¹ Ofloxacin, 20 mg L ⁻¹	40% (120 min) 97% (120 min)	[115]
P-g- C_3N_4	Melamine	Phosphoric Acid	Thermal Polymerization	-	Visible	Dinotefuran, 2 mg L ⁻¹	40.6% (5 h)	[123]
	Melamine	Phosphoric Acid	Solvothermal	1.66	Visible	p-Hydroxybenzoic Acid, 1 mg L ⁻¹	77.3% (120 min)	[117]
S-g- C_3N_4	Melamine	Thiourea	Thermal Polymerization	2.51	Visible	Rhodamine B, 10 mg L ⁻¹	29.7% (30 min)	[121]
S-Cl-g- C_3N_4	Melamine	Thiourea and Ammonium Chloride	Thermal Polymerization	2.55	Visible	Rhodamine B, 10 mg L ⁻¹	100% (30 min)	[121]
Si-g- C_3N_4	Urea	Ammonium Fluorosilicate	Thermal Polymerization	2.75	Visible	Rhodamine B, 10 mg L ⁻¹	75% (50 min)	[118]

Halogen doping of g- C_3N_4 has also been reported in the literature and shows interesting results. In the case of chlorine doping of g- C_3N_4 , interesting aspects regarding the roles of interstitial and substitutional incorporation have been studied [120]. Substitutional chlorine doping may correspond to a higher specific surface area and oxidation performance, while the interstitial presence of chlorine contributes to a higher separation of photogenerated species. Thus, as both can occur simultaneously, their balanced doping may correspond to an optimization of the catalyst activity. The synthesis method applied and other parameters, such as the agitation and dopant ratio, can be fundamental to allow better control of the catalyst's characteristics. Moreover, as indicated previously during the discussion of other catalysts, halogen doping studies are very scarce, possibly due to their more difficult impregnation, being highly electronegative elements, and producing toxic by-products.

3.3.4. Co-Doping

The use of multiple elements simultaneously for the doping of g- C_3N_4 has already been explored, albeit with fewer studies, and has shown a great boost in the material photoactivity. The most significant feature of g- C_3N_4 co-doping is appointed to be an improvement in electron mobility [119]. Moreover, additional alterations also promote the increase in the material photocatalytic performance, such as modifications of its morphology. The use of different amounts of dopants may dictate the final structure of the catalyst, as found by Ganganboina et al. [119], where an increasing amount of phosphoric acid mL in the B-P-g- C_3N_4 synthesis transformed a solid into a sponge-like, and finally, a hexagonal tubular structure, which possessed a higher photoactivity (Figure 7). The hydrolysis of melamine, the g- C_3N_4 precursor, led to the production of cyanuric acid, which may form a supramolecular precursor complex involving both chemicals, and finally aggregate to form the catalyst structure. The dopants introduced may then adsorb on these supramolecular complexes and alter their configuration.

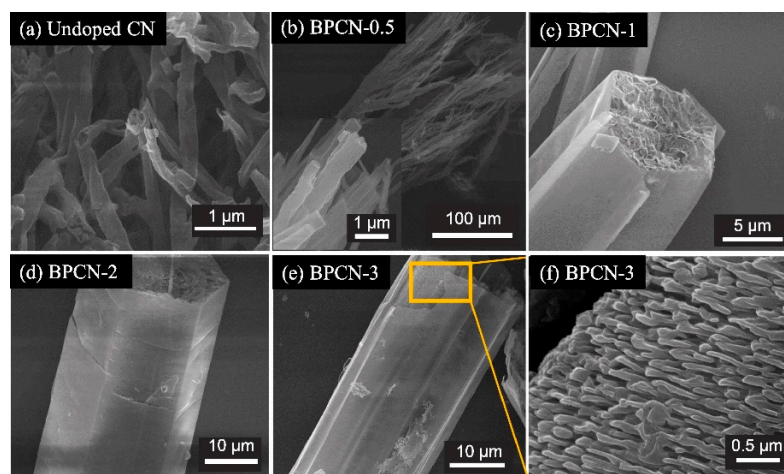


Figure 7. SEM images of (a) undoped $g\text{-C}_3\text{N}_4$, (b) 0.5 B-P- $g\text{-C}_3\text{N}_4$, (c) 1 B-P- $g\text{-C}_3\text{N}_4$, (d) 2 B-P- $g\text{-C}_3\text{N}_4$, (e) 3 B-P- $g\text{-C}_3\text{N}_4$, and (f) enlarged inside structure of 3 B-P- $g\text{-C}_3\text{N}_4$. (Retrieved with permission from Ref. [119] Copyright (2021) Elsevier).

3.4. Overall Considerations

The application of catalyst doping is a well-researched subject, noticeably producing positive effects regarding the improvement of photocatalytic activity. However, even with promising results, some considerations must be taken.

The similarities between the structures of WO_3 and TiO_2 as metal oxides allow analogous modification mechanisms to occur, providing great support as TiO_2 is already the subject of a great amount of research and information as it has been intensively optimized.

Rare-earth and noble metals provide excellent alterations, especially on the crystalline and electronic structure, due to the existence of more electron-rich orbitals, as well as their optical properties, e.g., through surface plasmon resonance. However, the sometimes complex and difficult impregnation of such elements, and their typically higher cost, need to be evaluated, although their use in small quantities can already provide significant results.

Other metallic elements can be an easier alternative, with comparatively lower costs regarding materials and impregnation techniques. In the case of $g\text{-C}_3\text{N}_4$, the exploration of transition metals doping is more widely explored, possibly due to the more distinct nature between the foreign and existent elements, which can provide more evident effects. These elements may lead to the easier formation of new energy sublevels and shift the light absorption to higher wavelengths. Such electronic interaction, especially as it occurs mainly with the conduction band of the catalysts, is also a great improvement for the less negative conduction band of WO_3 , which difficult its reduction potential. The ozone radical formation can also be enhanced by the modification of the conduction band, in the case of photocatalytic ozonation, facilitating the capture of electrons by ozone.

Nonetheless, transition metals doping has been reported to occasionally cause the lixiviation of such elements, e.g., iron and some heavy metals, presenting dangerous toxic effects and strict limits. Some progress in this matter has been made, with encapsulation techniques and methods that result in a stronger fixation, although it may increase the complexity of the process.

As the most abundant elements in nature, non-metals are the most broadly used elements in catalyst doping. Another great advantage is that a one-step method can usually be applied, simplifying the material's synthesis. Especially for $g\text{-C}_3\text{N}_4$, already being usually synthesized through a simple thermal polymerization, some compounds possess structures containing carbon and nitrogen together with other elements, which can be singularly applied, such as thiourea. Their electronic alteration may result in modification regarding the valence band, contributing, for example, to the less positive VB of $g\text{-C}_3\text{N}_4$ and improving hydroxyl radical production. Nonetheless, interaction with both conduction and valence bands can occur, even simultaneously, e.g., in sulfur doping.

In such a context, doping techniques represent a simple approach to overcome typical catalyst disadvantages and improve their performance. The difference in overall studies can challenge the conceptualization of standard knowledge, as multiple features can be altered and conflicting data exist. Thus, a more precise study may be necessary to evaluate each case.

4. Composite Catalysts

With the increasing conceptualization of different catalysts, the combination of different materials emerges to present a wide number of possibilities to improve the overall catalytic properties [124]. By mixing materials with different characteristics, their individual disadvantages may be overcome, and a final and more robust photocatalyst can be obtained. These composites are then a combination of materials with distinct natures, such as mixed metal oxides, carbon-semiconductors, polymeric structures, porous materials, and many others. In this section, an overview of the principal applications of the previously discussed photocatalysts in composite materials will be discussed [125]. The use of WO_3 , $\text{g-C}_3\text{N}_4$, and TiO_2 combined in different composite catalysts is evaluated in Table 7.

The mixing of WO_3 and TiO_2 is a clear example of mixed metal oxides, a well-known group of photocatalysts defined by the combination of different semiconductors. The coupling of these photocatalysts aims to improve the photocatalytic activity of the resultant material by mostly increasing the charges separation efficiency and visible-light sensitization for the complete system [125]. Mugunthan et al. [126] proved the higher efficiency of the coupled TiO_2/WO_3 catalyst for diclofenac elimination under visible radiation. The group synthesized the photocatalyst through a hydrothermal method and studied the variation of $\text{TiO}_2:\text{WO}_3$ molar ratios. The composites presented higher surface areas and smaller particles compared to bare TiO_2 , with the increasing amount of TiO_2 leading to larger S_{BET} , but also particle sizes, and E_{bg} . Thus, an optimum $\text{TiO}_2:\text{WO}_3$ molar ratio (10:1), presented more balanced properties and higher removal of diclofenac (~90%). An excess amount of WO_3 is also appointed to possibly act as recombination centers for the photoinduced charges, reducing the process efficiency.

The surplus addition of one of the applied semiconductors can also promote the agglomeration of photocatalyst particles, which may hinder the absorption of light and CECs photodegradation, as it was suggested by El-Yazeed and Ahmed [127] during the impregnation of WO_3 particles onto TiO_2 , which had a detrimental effect over a concentration of 10 wt%. This was also found by Wang et al. [128] for hollow spherical TiO_2/WO_3 composite, with uniform spheres being formed with a 5 wt% incorporation of WO_3 , but with the further increase in concentration and particle agglomeration causing changes in the catalyst morphology and leading to flat and unequal forms. However, in this study, the catalyst containing 10 wt% WO_3 had a better performance in methylene blue and metoprolol degradation, due to the photoelectronic and surface area improvements.

The $\text{TiO}_2\text{-WO}_3$ heterojunction can greatly improve the photo-mechanisms involved in the photocatalytic process. Considering their bandgap positions, the charge separation can follow two mechanisms: type-II heterojunctions or Z-scheme mechanisms (Figure 8). For the type-II mechanism, the excited electrons from the CB of TiO_2 , which has a more negative potential, will migrate to the CB of WO_3 . Meanwhile, the opposite occurs in the positive holes, which tend to be transferred to the TiO_2 VB [129]. Nonetheless, the Z-scheme mechanism is appointed to be more favorable due to the larger redox potential, as the e^- of the CB of WO_3 and h^+ of the VB of TiO_2 tend to recombine fast, leading to the accumulation of e^- on the CB of TiO_2 and h^+ on the VB of WO_3 , potentializing its respective reductive and oxidative potential [130].

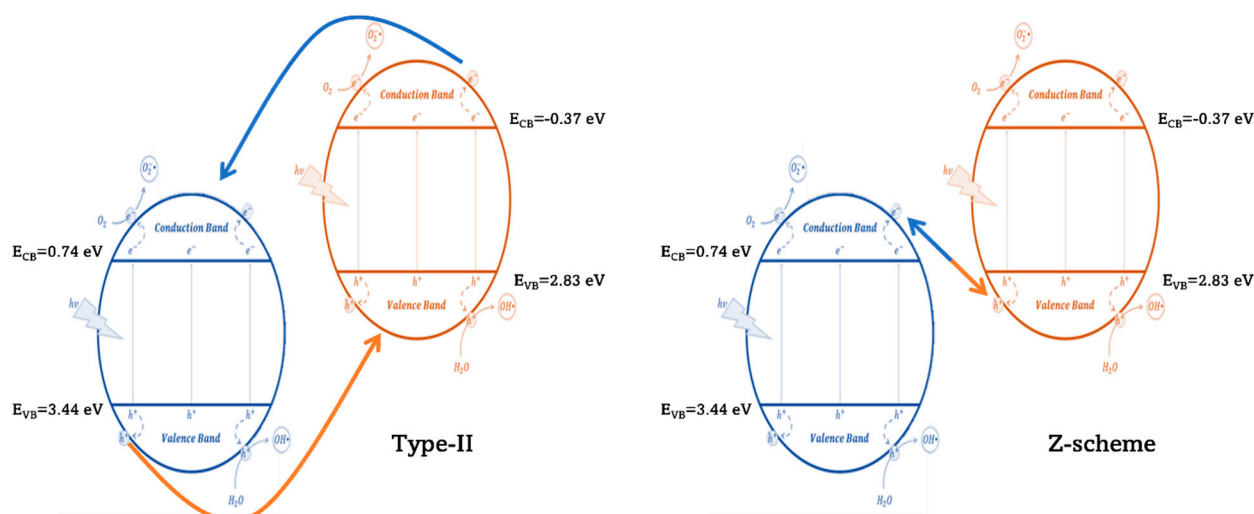


Figure 8. Representation of the mechanisms of Z-scheme and type-II heterojunctions [130–132].

Moreover, Wei et al. [131] indicated that, during the degradation of malachite green under visible light using $\text{TiO}_2\text{-WO}_3$, the superoxide radical ($\cdot\text{O}_2^-$) was one of the main mechanisms of the contaminant removal, even with the characteristic disadvantage of the more positive CB potential of WO_3 (0.74 eV vs. NHE) comparatively to the redox potential of $\cdot\text{O}_2^-/\text{O}_2$ (−0.33 eV vs. NHE). Thus, the composite material may also take advantage of alterations of the carriers' transference through interactions with TiO_2 , allowing the adsorption and reduction of oxygen.

The use of doped catalysts in the coupled systems can further improve the overall efficiency through the synergic effect between all species. For instance, the use of noble metals, which promote the surface plasmon resonance effect, or non-metals that can increase visible light absorption, alongside the lower e^-/h^+ recombination and electronic bands interaction of the heterojunction can potentialize contaminants removal [133,134].

More complex composites may be synthesized by the continuous arrangement of materials with different natures. Chen et al. [135] combined carbon-based and ceramic materials with metal oxides, producing silica- TiO_2 microspheres coupled with graphene oxide (GO) and WO_3 quantum dots. Each material has a principal role, and the arrangement is conducted to overcome their individual drawbacks. GO possesses large surface areas and good electrical properties and may enhance the photocatalytic activity of semiconductors as it does not present one on its own. Meanwhile, silica is a low-cost and non-toxic template, and WO_3 and TiO_2 may harness the beneficial effects of their coupled mechanisms. Finally, the complex composite presented enhanced optoelectrical properties and higher photocatalytic activity under natural sunlight, removing 98% of RhB under 60 min.

The polymeric characteristics of $g\text{-C}_3\text{N}_4$ can also be greatly advantageous when coupled with other semiconductors and materials. The metal-free catalyst exhibits narrower bandgap energy, making the photoexcitation of the electrons in the VB under visible light possible. Nonetheless, one of its main drawbacks is the low VB potential, which typically lies below the redox potential for the reaction between positive holes and water to occur, producing hydroxyl radicals.

Following computational density functional theory (DFT) calculations, Deng et al. [136] investigated the $g\text{-C}_3\text{N}_4/\text{TiO}_2$ heterostructure. The study proposed that the composite may present a lower E_{bg} than the single catalysts. Moreover, it was found that an accumulation of photogenerated electrons over the CB of $g\text{-C}_3\text{N}_4$ occurred, while positive holes tended to accumulate on the VB of TiO_2 , meaning that reduction reactions will favorably take place on $g\text{-C}_3\text{N}_4$, and oxidation will occur on TiO_2 . These mechanisms may also reduce the recombination of the photogenerated pairs and lead to higher radical production, especially $\cdot\text{OH}$, due to the well-constructed heterojunction [137].

Table 7. Application of WO₃, g-C₃N₄, and TiO₂ mixed composites for photocatalytic removal of contaminants.

Composite	S _{BET} (m ² g ⁻¹)	E _{bg} (eV)	Radiation Source	Contaminant	Removal (Time)	Ref.
g-C ₃ N ₄ /TiO ₂	200.0	2.70	UV	Formic Acid, 50 mg L ⁻¹	90.0% (5.5 h)	[138]
	40.2	2.81	Solar	Methylene Blue, 10 mg L ⁻¹	94.9% (80 min)	[137]
				Rhodamine B, 15 mg L ⁻¹	93.1% (80 min)	
	-	-	Visible	<i>E. coli</i> , 10 ⁷ CFU mL ⁻¹	100% (180 min)	[139]
-	2.58	Solar	<i>E. coli</i> , 10 ³ CFU mL ⁻¹	96.8% (30 min)	[140]	
WO ₃ /TiO ₂	88.4	3.06	Visible	Malachite Green, 50 mg L ⁻¹	99.0% (60 min)	[131]
	11.7	2.40	Visible	Methylene Blue, 10 mg L ⁻¹	87.8% (150 min)	[128]
				Metoprolol, 2 mg L ⁻¹	67.1% (150 min)	
103.9	2.95	Visible	Diclofenac, 10 mg L ⁻¹	100% (150 min)	[126]	
WO ₃ /g-C ₃ N ₄	-	-	UV-A + Visible + NIR	Ciprofloxacin, 10 mg L ⁻¹	98.6% (180 min)	[141]
	-	-	-	Tetracycline, 10 mg L ⁻¹	98.5% (180 min)	
	28.6	2.53	UV + Visible	Tartrazine, 25 mg L ⁻¹	95.0% (20 min)	[142]
S-doped g-C ₃ N ₄ /TiO ₂	-	3.00	Visible	Tetracycline, 10 mg L ⁻¹	98.1% (60 min)	[143]
N-doped CHS/g-C ₃ N ₄ /TiO ₂	78.0	-	Visible	Tetracycline, 20 mg L ⁻¹	85.0% (120 min)	[144]
Ag ₃ PO ₄ /g-C ₃ N ₄ /TiO ₂	-	2.07	Visible	Metronidazole, 8.2 mg L ⁻¹	97.2% (60 min)	[145]
C-doped WO ₃ /TiO ₂	93.0	2.98	Solar	Diclofenac, 10 mg L ⁻¹	100% (250 min)	[133]
Ag-doped WO ₃ /TiO ₂	-	3.07	Visible	Methylene Blue, 3.2 g L ⁻¹	72% (60 min)	[134]
GO/WO ₃ /TiO ₂	-	2.89	Solar	Rhodamine B, 143.7 mg L ⁻¹	98.2% (5 h)	[146]
	-	-	Solar	<i>E. coli</i> , 2 × 10 ³ CFU mL ⁻¹	97.3% (80 min)	[147]
CQDs/WO ₃ /TiO ₂	96.2	2.61	Solar	Cephalexin, 10 mg L ⁻¹	100% (90 min)	[148]
GO/CQDs/WO ₃ /TiO ₂ /SiO ₂	202.6	-	Solar	Rhodamine B, 14.4 mg L ⁻¹	98% (60 min)	[135]
Cd-doped WO ₃ /g-C ₃ N ₄	8.5	1.53	Visible	Methylene Blue, 10 mg L ⁻¹	96.0 (80 min)	[93]

The WO₃/g-C₃N₄ can thus be an interesting coupled system, as both catalysts can benefit from the synergic effect regarding their energy band potential and radical production. Huang et al. [141] produced g-C₃N₄ nanosheets coupled with WO₃ quantum dots (QDs), and they indicated that the combination of a strong reducing capacity of the CB of g-C₃N₄ to react with electron acceptors, such as O₂ and O₃, combined with the oxidation ability of the VB of WO₃ to form ·OH, promoted a greatly improved photocatalytic activity towards tetracycline and ciprofloxacin, with removals higher than 98%. Furthermore, the WO₃ QDs induced a local surface plasmon resonance, enhancing the charge carrier's separation efficiency.

Besides the reduction of E_{bg} and the synergic effect over photogenerated carriers, morphology modification may also be obtained to suppress the usual low specific surface area of g-C₃N₄. The coupling of g-C₃N₄ with TiO₂, WO₃, or other materials may lead to the formation of different porous structures and the existence of multiple functional groups that may interact with a wider range of organic pollutants [93,149].

In the following sections, the use of TiO₂, g-C₃N₄, and WO₃ in different composite materials as well as their main and most recently found advantages and mechanisms will be assessed.

4.1. TiO₂

Over the years, TiO₂ was vastly employed in the production of different composite catalysts, allowing a better understanding of their overall mechanisms and advantages.

The coupling of TiO₂ with other photocatalytic materials appeared as a vast family of mixed catalysts, with combined improved properties. Due to the existence of multiple photocatalysts, numerous combination possibilities are the aim of a rising number of investigations. Some studies involving TiO₂ composite catalysts are present in Table 8.

Zinc Oxide (ZnO) is, jointly with TiO₂, one of the most investigated semiconductors for contaminants removal, sharing their good photochemical characteristics but with relatively better electrical properties. Nonetheless, their heterostructures have been explored in different forms and systems for pollutant elimination. The increasing addition of ZnO in ZnO/TiO₂ fibers has been shown to also promote changes in the physical properties of the material, creating a rougher surface with a higher specific surface area and faster interaction with contaminants [150]. Changes in the morphology of the material have been also attested. Das et al. [151], indicated the transformation of uniform rod-like structures of ZnO into more of a flower-like form by the addition of TiO₂, with the enhancement of the BET surface until an optimal amount. A lower recombination rate of the electron-hole pairs was also demonstrated, increasing the lifespan of the photoinduced charge carriers.

The combination of TiO₂ with bismuth-based materials is a topic that gained much attention, as this family of compounds presents a series of attractive features, such as their low toxicity, easy functionalization, cost-effectiveness, and ability to absorb in near infra-red regions. Some examples of the most studied Bi-based photocatalysts are bismuth oxide (Bi₂O₃), bismuth vanadate (BiVO₄), and bismuth oxyhalide (BiOX), involving combination with halogen elements (X) [152–154].

The BiVO₄/N-TiO₂ heterostructure synthesized by Cipagauta-Díaz et al. [152] presented increased specific surface areas and absorption of visible light with the increasing BiVO₄ content. The catalyst also presented zones of heterogeneity that allow contact between the semiconductors and improve the separation of photogenerated charges and the lifetime of charge carriers. Ultimately, the best composite catalyst resulted in 98% removal of ofloxacin under 90 min. Even with the morphology and light absorption properties improvement, an excessive amount of BiVO₄ (>5 wt%) was demonstrated to be prejudicial to the photocatalytic performance, possibly due to the formation of BiVO₄ agglomerates in the catalyst surface, which hamper the homogeneous light absorption.

The electron-accepting nature of Bi₂O₃ was also proven to enhance the lifetime of the photocarriers and considerably increase the visible light absorption, even if the E_{bg} of the resulting materials did not suffer great alteration. Sharma et al. [153] indicated that Bi₂O₃ creates heterojunctions that facilitate the transport of photogenerated carriers and improve the visible light-capturing capacity in a CuO/Bi₂O₃/TiO₂ ternary composite catalyst. However, in high concentrations, Bi₂O₃ can reduce the catalyst efficiency, as pure Bi₂O₃ possesses less activity and can act as a recombination center.

Table 8. Application of TiO₂ composites for photocatalytic removal of contaminants.

Composite	S _{BET} (m ² g ⁻¹)	E _{bg} (eV)	Radiation Source	Contaminant	Removal (Time)	Ref.
ZnO/TiO ₂	-	3.15	UV	Eriochrome Black T, 6.4 × 10 ³ mg L ⁻¹	82% (6 h)	[155]
	84.7	3.15	Solar	Methylene Blue, 6.4 mg L ⁻¹ Methyl Orange, 6.5 mg L ⁻¹	95% (60 min) 99% (60 min)	[151]
BiVO ₄ /N-TiO ₂	92.0	2.56	Visible	Ofloxacin, 20 mg L ⁻¹	98% (90 min)	[152]
				Rhodamine B, 20 mg L ⁻¹	92% (90 min)	
Bi ₂ O ₃ /TiO ₂	102.9	-	Visible	Rhodamine B, 10 mg L ⁻¹	100% (100 min)	[153]
CuO/Bi ₂ O ₃ /TiO ₂	83.6	-	Visible	Rhodamine B, 10 mg L ⁻¹	100% (60 min)	

Table 8. Cont.

Composite	S_{BET} ($\text{m}^2 \text{g}^{-1}$)	E_{bg} (eV)	Radiation Source	Contaminant	Removal (Time)	Ref.
$\text{Fe}_2\text{O}_3/\text{TiO}_2$	-	2.49	Solar	Methylene Blue, 10 mg L^{-1}	92% (180 min)	[156]
	-			Phenol, 10 mg L^{-1}	52% (180 min)	
	56.9	3.08	Visible	Naproxen and Ibuprofen, 10 mg L^{-1} each	100% NPX (15 min) and 91% IBF (240 min)	[157]
$\text{Au}/\text{Fe}_2\text{O}_3/\text{TiO}_2$	-	1.55	Visible	2,4 Dichlorophenol, 10 mg L^{-1}	94% (90 min)	[158]
	-	1.55	Visible	4-Bromophenol, 10 mg L^{-1}	97% (60 min)	
$\text{SiO}_2/\text{Fe}_3\text{O}_4/\text{Sn-TiO}_2$	-	1.32	UV	Tetracycline, 10 mg L^{-1}	98.2% (40 min)	[159]
	-	-	-	<i>E.coli</i> , 10^7 CFU mL^{-1}	100% (20 min)	
$\text{P}/\text{Ag}/\text{Ag}_2\text{O}/\text{Ag}_3\text{PO}_4/\text{TiO}_2$	307.2	2.98	Visible	<i>Salmonella</i> , 10^7 CFU mL^{-1}	100% (30 min)	[160]
				<i>Enterococcus sp.</i> , 10^7 CFU mL^{-1}	100% (6 h)	
				<i>S. aureus</i> , 10^7 CFU mL^{-1}	100% (3 h)	
				-	-	
$\text{CNT}/\text{Au-TiO}_2$	-	1.95	Solar	Methylene Blue, 3 mg L^{-1}	80% (30 min)	[161]
GO/TiO_2	-	3.02	Solar	<i>E. coli</i> , 10^7 CFU mL^{-1}	99.9% (30 min)	[162]
$\text{Chitosan}/\text{N-TiO}_2$	52.0	2.82	UV	Patulin, $500 \mu\text{g kg}^{-1}$	100% (35 min)	[163]
$\text{Perlite}/\text{F-Ce-TiO}_2$	14.8	2.96	Visible	<i>Microcystis aeruginosa</i> , $2.7 \times 10^6 \text{ cell mL}^{-1}$	98.1% (9 h)	[164]

Iron oxides (e.g., Fe_2O_3 , Fe_3O_4) have been successfully used in photocatalytic systems, as highly chemically stable and non-toxic materials with narrow bandgaps and interesting magnetic properties [124]. $\alpha\text{-Fe}_2\text{O}_3$ possesses a broad absorption over the entire UV-Vis region. Thus, their use in composite photocatalytic can significantly extend the material's optical absorption, allowing it to preserve a good photocatalytic activity in both UV and visible range, and fully harness solar radiation (Figure 9) [165]. Bouziani et al. [156] demonstrated the expansion of absorption range in sol-gel synthesized $\alpha\text{-Fe}_2\text{O}_3/\text{TiO}_2$, as single TiO_2 presented minimal absorption over 400 nm while the composite catalyst showed good absorption over all UV-Vis spectra. Furthermore, the 10 wt% $\alpha\text{-Fe}_2\text{O}_3/\text{TiO}_2$ had better crystallization and a greater number of active sites, providing a faster degradation of methylene blue and phenol, i.e., 96% and 52%, within 120 min of sunlight irradiation.

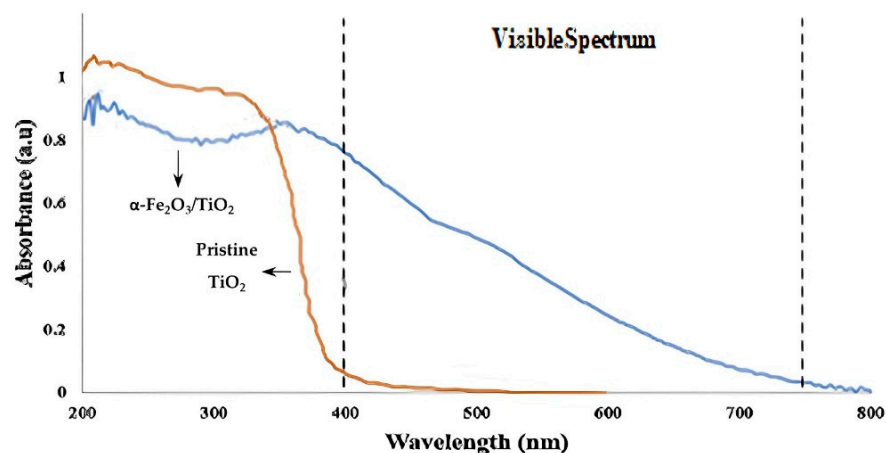


Figure 9. UV-vis spectra of $\text{Fe}_2\text{O}_3/\text{TiO}_2$ composite and commercial TiO_2 (Adapted and retrieved with permission from Ref. [162] Copyright (2020) Elsevier).

The synthesis of $\alpha\text{-Fe}_2\text{O}_3/\text{TiO}_2$ composites may also occur using metal-organic frameworks (MOFs) as sacrificial templates. These materials are highly porous and lead to the

formation of homogeneous structures with excellent electronic mobility and active sites. Li et al. [158] confirmed the potential of these catalysts through the study of MOF-derived Au-doped α -Fe₂O₃/TiO₂ and its reaction with 2,4 dichlorophenol and 4-bromophenol. The ternary system obtained degradation rates higher than 95% in 90 min, accounted for the high surface area and the number of reactive sites, and the movement of excited electrons between the more negatively charged CB of TiO₂ to the CB of Fe₂O₃ in the formed heterojunction. Peña-Velasco et al. [157] also concluded that, when synthesizing a Fe₂O₃/TiO₂ composite derived from a Fe-based MOF (MIL-101), Fe³⁺ may partially substitute Ti⁴⁺ in the TiO₂ structure, which may introduce lattice defects and vacancies that boost the photocatalytic activity, achieving 91% and 100% removal of ibuprofen and naproxen.

Asgari et al. [53] reported the efficient use of magnetic Fe₃O₄/TiO₂ composite catalyst in photocatalytic ozonation reactions. The presence of the photocatalyst enhanced ozone decomposition in the medium and the generation of oxidative radicals, boosting the degradation of ceftazide, eliminated under 15 min with a reaction rate constant of 0.1682 min⁻¹, almost two times faster than single ozonation. The magnetic property of the composite may also facilitate the posterior removal of the catalyst from the medium, a key parameter for the scale-up of the process. Remarkably, Lu et al. [159] appointed that interference may occur in the Fe₃O₄/TiO₂ catalyst as a result of Fe ion diffusion to the surrounding TiO₂, causing excessive doping. The authors utilized a SiO₂ coating, as a ceramic material able to shield the Fe₃O₄, but also reduce particle agglomeration, forming a ternary composite.

Carbonaceous materials, such as carbon nanotubes (CNTs), carbon quantum dots (CQDs), activated carbon (AC), and graphene oxide (GO), can provide support for the photocatalyst, but also great mechanical and electrical properties that may enhance its photoactivity. CNTs possess high mechanical strength and conductivity, but also present an important charge storage capacity and can act as a receiver of the photogenerated electrons from the catalyst CB. Mohammed [161] indicated an incredibly higher specific surface area of CNT/Au-TiO₂ hybrid catalysts, in simultaneous to higher absorption of visible light, effective transport of charges between CNTs and TiO₂, reduced electron-hole pair recombination, and better adsorption of molecules. CNTs may also promote a higher ozone decomposition in photocatalytic ozonation reactions, as ozone present a high affinity towards basic carbons due to its high density of π electrons on the basal planes. Orge et al. [166] verified the higher efficiency of CNT/TiO₂ in the photocatalytic ozonation of oxamic acid, which was completely removed under 60 min. The group also pointed out that ozone decomposition may be favored by CNTs with low acidic characteristics.

Graphene oxide (GO) also shows appealing hydrophilic features, tunable attributes, and particular optical properties that may be applied to composite materials. Different GO-hybrid catalysts have shown better exploitation of visible and solar irradiation, fast electron transference, and suppressed agglomeration. Thomas et al. [162] exploited the antibacterial properties of GO in GO/BiVO₄ and GO/TiO₂ composites, with a higher production of ROS and the characteristic morphology, small size, and sharp edges. Both binary composites presented promising results regarding their application in disinfection treatment. However, GO/TiO₂ had a better performance with a 3-log reduction of *E. coli* K12. It was indicated that Bi ions interactions with the surface of bacteria cells are lengthier than with Ti ions, which can bind to the glycoproteins and penetrate the cell.

In ozone-assisted photocatalysis, Chávez et al. [167] combined the magnetic properties of Fe₃O₄ and the high surface area of activated carbon (AC) with a TiO₂ catalyst for the treatment of a real secondary effluent spiked with different CECs. The study proved the higher efficiency of photocatalytic ozonation, as single ozonation presented low mineralization levels and photocatalytic oxidation did not achieve the full elimination of CECs. Thus, the combined process showed faster removal, lower presence of intermediates, and better usage of ozone. Nonetheless, it was appointed that interactions between ozone and AC may alter the latter surface chemical properties, as a pH_{ZPC} decrease was found because of acidic oxygen groups on the surface of the carbon structure. This modification may affect

the adsorptive behavior of the material. Other studies involving the application of TiO₂ composites in photocatalytic ozonation treatments are present in Table 9.

Table 9. Application of TiO₂ composites in photocatalytic and ozone-based processes for contaminants removal.

Composite	Radiation Source	Contaminant	Oxidant	Results	Ref.
CNT/TiO ₂	UV	Oxamic acid, 89 mg L ⁻¹	O ₂	70% removal in 60 min	[166]
			O ₃	100% removal in 60 min	
			-	24% removal in 60 min	
Fe ₃ O ₄ /TiO ₂	UV-A	Ceftazide, 10 mg L ⁻¹	O ₂	34.6% removal in 15 min	[168]
			O ₃	100% removal in 15 min	
			-	86.7% removal in 15 min	
AC/Fe ₃ O ₄ /TiO ₂	Solar	Metoprolol, Ibuprofen, Clofibric acid and DEET, 2 mg L ⁻¹ each	O ₂	56% and 45% removals of contaminants mixture in 120 min in, respectively, synthetic and real secondary effluent, and up to 40% of DOC removal	[167]
			O ₃	100% removal of contaminants mixture in 15 min and up to 70% of DOC removal	
			-	100% removal of contaminants mixture in 30 min and up to 25% of DOC removal	
GO/Fe ₃ O ₄ /TiO ₂	Solar	Cotinine, Caffeine, Ciproflaxin, Metoprolol, Sulfamethoxazole, Bezafibrate, Tritosulfuron, Ibuprofen, Clofibric acid, and DEET, 0.5 mg L ⁻¹ each	O ₃	70% of TOC removal in 120 min at pH = 4 in urban wastewater	[169]
			-	63% of TOC removal in 120 min at pH = 4 in urban wastewater	

4.2. WO₃

To overcome WO₃ drawbacks and obtain a more robust photocatalytic material, various hybrid structures have been explored. The coupling with other metal oxides and semiconductors is more substantially pursued, possibly as a more facile approach to surpass its high electron-hole recombination rate, and the less negative conduction band and compromised reductive potential, as it can benefit from the electron-hole interaction of the formed heterojunctions. The use of these WO₃ composites in the degradation of different contaminants is demonstrated in Table 10.

In recent years, phosphate-based photocatalysts, especially Ag₃PO₄, have been the focus of numerous studies due to their superior quantum efficiency under visible light irradiation, 90% [22]. However, it still faces relatively large particle sizes (0.5–2 μm), instability, and photo-corrosion, hindering a highly efficient photoactivity and its recyclability. Thus, Ag₃PO₄ and WO₃ composites may benefit from their heterostructures and be presented as more robust photocatalysts. Liu et al. [170] demonstrated that Ag₃PO₄/WO₃ had relatively stronger absorption in the long-wavelength range (>500 nm), while single WO₃ presented no activity in the same range. Regarding the ratio between the semiconductors, when Ag₃PO₄ exceeded 60%, a decrease in the photocatalytic activity towards RhB degradation, related to an excessive number of Ag₃PO₄ particles deposited at the WO₃ surface that may block light penetration. However, other studies showed that the formation of metallic Ag during the composite synthesis may occur and possess a negative effect, inhibiting the transport of positive holes from the Ag₃PO₄ VB to its surface, and the deposition of inactive substances over the composite surface, blocking active sites [171].

The instability of Ag₃PO₄ can be further increased by adding other components with better electronic properties. Graphene, which can be doped to boost its characteristics, is an excellent electron mediator and has been demonstrated to significantly increase the recyclability of Ag₃PO₄/WO₃ composites, providing higher chemical stability, surface area, and electron mobility by the organic material on the ternary composite [172].

Other semiconductors have been combined with WO₃, as mentioned, effectively obtaining improved features. Sodium niobate (NaNbO₃) is a semiconductor with a perovskite

structure, low density, and high crystallinity, but with a broad bandgap energy (3.0–4.7 eV). The respective $\text{NaNbO}_3/\text{WO}_3$ has been reported to possess great photocatalytic activity, with a higher separation of photogenerated charges and reductive potential, benefiting from the considerably more negative conduction band of NaNbO_3 [173]. ZnWO_4 is another photocatalyst that presents higher bandgap energy (3.5–5.7 eV), but its formed composites with WO_3 can broaden its visible light absorption and form built-in electric fields as a result of a fast electron transference between both materials [174].

Table 10. Application of WO_3 composites for photocatalytic removal of contaminants.

Composite	S_{BET} ($\text{m}^2 \text{g}^{-1}$)	E_{bg} (eV)	Radiation Source	Contaminant	Removal (Time)	Ref.
$\text{Ag}_3\text{PO}_4/\text{WO}_3$	23.9	-	Visible	Rhodamine B, 20 mg L^{-1}	98% (90 min)	[170]
$\text{Ag}_3\text{PO}_4/\text{WO}_3 \cdot \text{H}_2\text{O}$	-	2.43	Visible	Methylene Blue, 10 mg L^{-1} and Tetracycline 20 mg L^{-1}	98.9% MB and 70.4% (35 min)	[171]
$\text{Ag}_3\text{PO}_4/\text{NG}/\text{WO}_3$	-	2.36	Visible	Indomethacin, 5 mg L^{-1}	99.3% (50 min)	[172]
$\text{NaNbO}_3/\text{WO}_3$	7.2	2.60	Visible	2,4-Dichlorophenoxyacetic acid, 10 mg L^{-1}	60% (210 min)	[173]
$\text{Bi}_2\text{S}_3/\text{WO}_3$	53.8	1.90	Visible	Rhodamine B, 10 mg L^{-1}	90.7% (100 min)	[175]
$\text{Ag}/\text{ZnWO}_4/\text{WO}_3$	-	-	UV-Visible	Methylene Blue, 200 mg L^{-1}	94% (80 min)	[174]
GO/ WO_3	18.7	2.32	Visible	Rhodamine B, 20 mg L^{-1}	96% (120 min)	[176]
				Ciprofloxacin, 20 mg L^{-1}	90% (120 min)	
$\text{Ag}/\text{GO}/\text{Chitosan}/\text{WO}_3$	26.4	2.40	Visible	Methylene Blue, 10 mg L^{-1}	99% (8 min)	[177]
$\text{SBA-15}/\text{Ag}-\text{WO}_3$	208	1.70	Visible	Atrazine, 20 mg L^{-1}	68% (18 min)	[178]

Gondal et al. [178] reported efficient herbicide removal using SBA-15, a highly porous siliceous material, as a template for a $g\text{-C}_3\text{N}_4$ composite catalyst, to obtain a structure with a high surface area and facilitate the reutilization of the material. The composite also benefits from the presence of the noble metal, with the surface plasmon resonance effect, which can increase light absorption, but it can also act as an electron trap center, as its Fermi level is lower than the semiconductor and electrons tend to accumulate on the Ag particles. Finally, the $\text{SBA-15}/\text{Ag}-\text{WO}_3$ presented a ~70% removal of atrazine, with a reaction rate constant of 0.065 min^{-1} .

4.3. $g\text{-C}_3\text{N}_4$

The characteristics of graphitic carbon nitride that hinder its broader utilization, such as its low specific surface area, obstructed active sites, and visible light utilization, can be strongly surpassed by the construction of composite materials. Its polymeric structure may be linked to other materials, with their own photocatalytic properties or characteristics that can boost the $g\text{-C}_3\text{N}_4$ performance. Their application in photocatalytic studies is shown in Table 11.

Table 11. Application of $g\text{-C}_3\text{N}_4$ composites for photocatalytic removal of contaminants.

Composite	S_{BET} ($\text{m}^2 \text{g}^{-1}$)	E_{bg} (eV)	Radiation Source	Contaminant	Removal (Time)	Ref.
$\text{Bi}_4\text{O}_7/g\text{-C}_3\text{N}_4$	109	-	Visible	<i>Aspergillus fumigatus</i> , 10^6 CFU mL^{-1}	81% (6 h)	[179]
$\text{BiVO}_4/g\text{-C}_3\text{N}_4$	7	2.43	Visible	Nonylphenol Ethoxylate, 50 ppm	100% (120 min)	[180]
$\text{BiVO}_4/\text{Bi}_2\text{O}_6/g\text{-C}_3\text{N}_4$	95.9	-	Visible	Rhodamine B, 20 mg L^{-1}	100% (60 min)	[181]
				Tetracycline, 20 mg L^{-1}	100% (60 min)	
$\text{LaVO}_4/g\text{-C}_3\text{N}_4$	-	-	Visible	Tetracycline, 20 mg L^{-1}	83.4% (30 min)	[182]
				Naproxen, 20 mg L^{-1}	80% (120 min)	
$\text{Ag-ZnO}/\text{S-g-C}_3\text{N}_4$	57.2	2.51	Solar	Methylene Blue, 10 mg L^{-1}	97% (40 min)	[183]

Table 11. Cont.

Composite	S_{BET} ($\text{m}^2 \text{g}^{-1}$)	E_{bg} (eV)	Radiation Source	Contaminant	Removal (Time)	Ref.
HTCC/O-g-C ₃ N ₄	-	0.95	Visible	Human Adenovirus Type 2, 10^5 MPN mL^{-1}	100% (120 min)	[184]
PAN/g-C ₃ N ₄	13.3	-	UV	Oilfield Produced Water	96.6% (8 h)	[185]
			Visible		85.4% (8 h)	
PEI/g-C ₃ N ₄	70.2	1.74	Visible	Tetracycline, 40 mg L^{-1}	80% (120 min)	[186]
PEI/g-C ₃ N ₄	-	-	Solar	<i>E. coli</i> , $2 \times 10^6 \text{ CFU mL}^{-1}$	100% (45 min)	[187]
				<i>Enterococcus faecalis</i> , $2 \times 10^6 \text{ CFU mL}^{-1}$	67.7% (60 min)	
Au-SiO ₂ /g-C ₃ N ₄	365	-	Visible	Rhodamine B, 10 mg L^{-1}	99.8% (90 min)	[188]
β -SiAlON/g-C ₃ N ₄	-	-	Visible	Murexide, 250 mg L^{-1}	90% (8 h)	[189]

There is an expanding number of studies regarding the combination of g-C₃N₄ with other polymeric materials. Their typically low-cost production, large surface areas, and presence of different functional groups and electrostatic charges can enhance pollutants interaction. Polyethyleneimine (PEI), for example, is a cationic polymer containing many amino groups that have been used in combination with catalyst and carbon-based materials to enhance the electrochemical properties and overall activity of composites. Yan et al. [186] synthesized in one step a PEI/g-C₃N₄ composite through the thermal copolymerization of urea mixed with PEI, obtaining a tremella-like structure containing -NH_x groups, that may be beneficial for water dispersion and photon absorption, and an increased BET surface area, up to 250%. The best composite catalyst also presented 80% removal of tetracycline with a reaction rate constant of 0.0226 min^{-1} , 3.2 times higher than g-C₃N₄. The efficiency of PEI/g-C₃N₄ has also been attested for disinfection purposes, by Zeng et al. [187], resulting in 6.2 and 4.2 log reductions of *E. coli* and *E. faecalis* in 45 and 60 min, respectively. PEI can increase O₂ reduction and alter the surface charges of the catalyst, promoting the adhesion of bacteria through electrostatic attraction.

Polyacrylonitrile (PAN) is also used for the synthesis of nanowires and other hybrid materials, with excellent flexibility and adsorption capacities. Alias et al. [185] applied electrospun PAN/g-C₃N₄ nanofibers for oilfield-produced water (OPW) treatment. The PAN matrix can adsorb organic compounds such as oil and accumulate them near g-C₃N₄, which allows the treatment of even more diluted solutions. The proposed composite obtained 96.6% and 85.4% degradation of OPW under UV and visible irradiation, respectively.

g-C₃N₄ has been used in combination with other metal oxides and semiconductor materials to merge its advantages and obtain heterojunctions with synergic effects. LaVO₄ and other vanadate complex oxides such as BiVO₄ present interesting features, especially their surface catalytic and optical properties, with good visible light absorption due to the V 3d orbital state. Jing et al. [182] indicated a high matching degree of LaVO₄ and g-C₃N₄ band structures in their respective hybrid catalyst, promoting an efficient migration of photocarriers and improving the photocatalytic activity. LaVO₄ also presents a more negative CB, while g-C₃N₄ has a more positive VB, potentializing the redox reactions in the respective bands of the heterostructure.

Dong et al. [180] demonstrated the advantages of BiVO₄ in combination with g-C₃N₄, which resulted in a material with a larger specific surface area, from 1.6 to $16.3 \text{ m}^2 \text{ g}^{-1}$, and better visible light absorption. The presence of bismuth precursors may cause the compression of g-C₃N₄, which facilitates electron transference to the catalyst surface and the photogenerated pair recombination [181].

The matching bands of Bi-based oxides and g-C₃N₄ catalysts, and their better reductive/oxidative potential and ROS production have been reported as efficient pathogens disinfection treatment. Zhang et al. [179] demonstrated the capacity of Bi₄O₇/g-C₃N₄ to eliminate germinated fungi spores of *Aspergillus fumigatus* under visible light, attaining

81% disinfection of an initial 1×10^4 CFU mL⁻¹. The boosted production of $\cdot\text{O}_2^-$ and $\cdot\text{OH}$ by the composite were fundamental for better performance, as they were appointed to be the main active species on the decomposition of the fungus cell wall and cytoplasm.

The significant improvement of treatment performance in photocatalytic ozonation using g-C₃N₄ composites has been also attested, and some studies are present in Table 12. Jourshabani et al. [190] investigated the Fe₂O₃ and S-g-C₃N₄ combination in a composite catalyst and obtained substantially higher mineralization of Bisphenol A (BPA) under visible radiation, 97.8% TOC removal in 3 h, compared with the photocatalytic oxidation and photolytic ozonation treatments, 41.1%, and 40.1% respectively. The presence of the Fe-based material enhances the visible light absorption of g-C₃N₄ and the adsorption of both contaminants and ozone, which leads to faster elimination, higher production of ROS, and lower dosages of ozone, consequently reducing the process cost.

Zhang et al. [184] reported the use of a metal-free heterostructure consisting of oxygen-doped g-C₃N₄ microspheres integrated with hydrothermal carbonation carbon (HTCC) for human adenovirus disinfection. HTCC is an interesting carbon-based material recently found to act as a visible-light semiconductor, with a lower cost production compared to other carbonaceous compounds, such as graphene, although it suffers from a low photocatalytic activity due to fast recombination of electron-hole pairs [191]. The group applied a facile solvo-hydrothermal method, and the resulting composite presented a robust photocatalytic performance and biocompatibility towards human cells, achieving 5-log inactivation of the virus within 120 min.

Table 12. Application of g-C₃N₄ composites in photocatalytic and ozone-based processes for contaminants removal.

Composite	Radiation Source	Contaminant	Oxidant	Removal (Time)	References
GO/g-C ₃ N ₄	Solar	Oxalic Acid, 10 mg L ⁻¹	O ₂	49.5% (40 min)	[192]
			O ₃	93.2% (40 min)	
			-	82% (40 min)	
SBA-15/Ag-g-C ₃ N ₄	Solar	Oxalic Acid, 10 mg L ⁻¹	O ₂	16.8% (11 min)	[193]
			O ₃	100% (11 min)	
			-	4% (11 min)	
Fe ₂ O ₃ /S-g-C ₃ N ₄	Visible	Bisphenol A, 50 mg L ⁻¹	O ₂	41.1% TOC (3 h)	[190]
			O ₃	97.8% TOC (3 h)	
			-	40.1% TOC (3 h)	

Ceramic materials may be employed in composite catalysts as highly porous materials with excellent mechanical properties. These materials also act as great templates for photocatalytic species, producing high surface areas and recycling properties. Akulinkin et al. [189] used β-SiAlON, an aluminosilicate porous material, as a base for a g-C₃N₄ composite. The semiconductor was loaded in the pores of the ceramic substrate and the catalyst was obtained in plate forms. The composite presented great removal of murexide dye, as a consequence of its extended surface area and stability, maintaining its photocatalytic activity after seven cycles.

5. Future Perspectives

TiO₂ is by far the most used photocatalyst and possesses its basic properties already optimized, with a proper position of its CB and VB, which allow good redox potentials, high crystallinity, and overall photocatalytic performance. Although some disadvantages still prevent its full application, such as fast electron-hole pair recombination and, more especially, its broad bandgap energy, which implies the use of UV irradiation.

Thus, the development of new visible light active photocatalysts has been extremely encouraged and studied by the scientific community. Among them, $g\text{-C}_3\text{N}_4$ and WO_3 appear as promising candidates, presenting lower bandgap energies, higher absorption of visible light, and still maintaining the required properties common to TiO_2 , such as good chemical stability and facile and low-cost production. Other alternative catalysts that have gotten more attention in recent years include the Bi-based (BiO_3 , BiVO_4 , BiOX) and phosphate (Ag_3PO_4 , CePO_4) catalysts, which have interesting visible-light and overall catalytic activities.

Even with a better performance in the visible region, these selected catalysts still suffer from low specific surface areas, high electron-hole pair recombination, and unfavorable band potential, as $g\text{-C}_3\text{N}_4$ typically presents low VB and WO_3 less negative CB potentials, that diminish, respectively, $\cdot\text{OH}$ production from water and O_2 reduction into $\cdot\text{O}_2^-$.

To overcome these obstacles, modifications of the photocatalysts can be explored, such as the introduction of multiple elements in catalyst doping, and the combination with materials of different natures to obtain composite photocatalysts. The incorporation of foreign elements in the structure of the catalyst may take place in different positions, with all possessing respective advantages. By the application of characterization methods, a specific analysis of each modification needs to be conducted to better understand its mechanisms. Generally, doping can alter the bandgap properties and may lead to shifts in the optical response of the catalysts, allowing it to present better responses towards higher wavelengths. These techniques may also reduce the photogenerated pairs recombination, modification of surface properties, and functional groups, which highly influence the interaction with CECs.

Composite materials encompass the use of mixed metallic oxides and other semi-conductors, ceramics, polymers, and other structures to obtain a combination of their individual strengths and advantages. Outstanding properties may be achieved, such as high specific surface areas, electron mobility, different morphologies, easier recyclability, posterior separation, and heterojunctions which may increase the reduction and oxidation reactions, an important aspect for the commented alternative catalysts.

Even so, each alteration may also have side effects. Possible poisoning, lixiviation, active site blockage, and loss of photoactivity may occur. Some compounds, such as noble metal or rare-earth elements, and more elaborated materials can also represent a high cost involved and short availability. The precise evaluation of the concentration of elemental dopants and added materials are crucial, with excessive doping resulting in the opposite effect, acting as recombination centers, or the extreme agglomeration of the structures in hybrid materials. The combination of different materials in composite catalysts may also lead to a faster deactivation of the final product, shortening their lifetime and increasing the process cost. Thus, a case-by-case analysis is fundamental to better understand these side effects and obtain a more tailored material, which can be an exhaustive task. Additionally, the catalysts' reuse and possible post-treatments for their reactivation need to be more profoundly explored.

The proper application and reactor to be used are also fundamental in the conceptualization of the photocatalytic treatment apparatus and need to be evaluated alongside the production of the catalytic material. This task is one of the greatest challenges, as it encompasses the optimization of multiple parameters, to ensure efficient light penetration, interactions between contaminants and the catalyst, proper residence time, etc. Even being a cost-free radiation source, sunlight photocatalyst activation may require special reactor designs, presenting additional costs that need to be evaluated case-by-case. Nonetheless, great advancements have been obtained in compound parabolic collector (CPC) reactor developments, allowing proper light penetration within the equipment and better exploitation of the photon source. A facile retrieval of the catalyst after the reaction is also a key factor and dependent on the selected reaction equipment. Some achievements have been obtained in this post-recovery phase, such as the exploitation of magnetic properties of some materials, which can assist in the separation and reutilization of the photocatalyst.

The number of studies involving the application of such materials in real effluents is considerably limited. There are different common parameters and compounds present in these complex water matrices that compromise and interact with the species participants in the photocatalytic ozonation reaction. Broader investigations are thus vital to understand these effects and construct a more robust system.

6. Conclusions

The application of semiconductors in photocatalytic based for CECs abatement has shown remarkable potential as a water treatment technology. The production of highly oxidative radicals may eliminate a variety of these chemical and biological compounds that represent a danger to human and environmental health. These treatments have been pointed out to be effective even in more complex matrices, which proves their capacity to be applied to real effluents under different conditions. The use of additional oxidants such as ozone can also boost the overall process efficiency, increasing the production of radicals and electron retrieval.

The investigations regarding new visible light active photocatalysts show promising results, but more complete studies still need to be conducted to collect more information. The applications of doping and composite materials open a great variety of possibilities for materials with more robust and feasible characteristics to be obtained. Thus, more elaborate comparisons between the new and standard semiconductors and their adaptations need to be performed, to better understand the advantages of further exploration of the already well-founded TiO₂ based materials and the development of alternative materials. The addition of ozone in the photocatalytic process has been proven to enhance the overall efficiency, and more studies of its application with alternative and adapted catalysts will be valuable. Nonetheless, the photocatalytic-based process is a favorable route for the degradation of pathogens and CECs and future large-scale water reclamation technologies.

Author Contributions: Conceptualization, E.F., J.G. and R.C.M.; methodology, E.F., J.G. and R.C.M.; writing—original draft, E.F.; writing—review and editing, J.G. and R.C.M.; supervision, J.G. and R.C.M.; funding acquisition, E.F., J.G. and R.C.M. All authors have read and agreed to the published version of the manuscript.

Funding: This work was financed by European Structural and Investment Funds through Portugal2020 by the project PhotoSupCatal—Development of supported catalytic systems for wastewater treatment by photo-assisted processes (POCI-01-0247-FEDER-047545). The authors gratefully acknowledge FCT (Fundação para a Ciência e Tecnologia, Portugal) for the PhD Grant (2020.06130.BD) and the financial support (CEECIND/01207/2018). Thanks are due to FCT/MCTES for the financial support to CIEPQPF (UIDB/00102/2020).

Data Availability Statement: Not applicable.

Conflicts of Interest: The authors declare no conflict of interest.

References

1. Gittins, J.R.; Hemingway, J.R.; Dajka, J.C. How a Water-Resources Crisis Highlights Social-Ecological Disconnects. *Water Res.* **2021**, *194*, 116937. [[CrossRef](#)]
2. Gleick, P.H. *The World's Water*; Island Press: Washington, DC, USA, 2015; Volume 8.
3. McCance, W.; Jones, O.A.H.; Cendón, D.I.; Edwards, M.; Surapaneni, A.; Chadalavada, S.; Wang, S.; Currell, M. Combining Environmental Isotopes with Contaminants of Emerging Concern (CECs) to Characterise Wastewater Derived Impacts on Groundwater Quality. *Water Res.* **2020**, *182*, 1–15. [[CrossRef](#)]
4. Rizzo, L.; Malato, S.; Antakyali, D.; Beretsou, V.G.; Đolić, M.B.; Gernjak, W.; Heath, E.; Ivancev-Tumbas, I.; Karaolia, P.; Lado Ribeiro, A.R.; et al. Consolidated vs New Advanced Treatment Methods for the Removal of Contaminants of Emerging Concern from Urban Wastewater. *Sci. Total Environ.* **2019**, *655*, 986–1008. [[CrossRef](#)]
5. Valbonesi, P.; Pro, M.; Vasumini, I.; Fabbri, E. Contaminants of Emerging Concern in Drinking Water: Quality Assessment by Combining Chemical and Biological Analysis. *Sci. Total Environ.* **2021**, *758*, 143624. [[CrossRef](#)]
6. Olalla, A.; Moreno, L.; Valcárcel, Y. Prioritisation of Emerging Contaminants in the Northern Antarctic Peninsula Based on Their Environmental Risk. *Sci. Total Environ.* **2020**, *742*, 140417. [[CrossRef](#)]

7. Lencioni, V.; Bellamoli, F.; Paoli, F. Multi-Level Effects of Emerging Contaminants on Macroinvertebrates in Alpine Streams: From DNA to the Ecosystem. *Ecol. Indic.* **2020**, *117*, 106660. [[CrossRef](#)]
8. Llamas-dios, M.I.; Vadillo, I.; Jiménez-gavilán, P.; Candela, L.; Corada-fernández, C. Assessment of a Wide Array of Contaminants of Emerging Concern in a Mediterranean Water Basin (Guadalupe River, Spain): Motivations for an Improvement of Water Management and Pollutants Surveillance. *Sci. Total Environ.* **2021**, *788*, 147822. [[CrossRef](#)]
9. Tian, Z.; Wark, D.A.; Bogue, K.; James, C.A. Suspect and Non-Target Screening of Contaminants of Emerging Concern in Streams in Agricultural Watersheds. *Sci. Total Environ.* **2021**, *795*, 148826. [[CrossRef](#)]
10. Shah, A.I.; Din Dar, M.U.; Bhat, R.A.; Singh, J.P.; Singh, K.; Bhat, S.A. Prospectives and Challenges of Wastewater Treatment Technologies to Combat Contaminants of Emerging Concerns. *Ecol. Eng.* **2020**, *152*, 105882. [[CrossRef](#)]
11. Liu, Z.; Demeestere, K.; Hulle, S. Van Comparison and Performance Assessment of Ozone-Based AOPs in View of Trace Organic Contaminants Abatement in Water and Wastewater: A Review. *J. Environ. Chem. Eng.* **2021**, *9*, 105599. [[CrossRef](#)]
12. Giwa, A.; Yusuf, A.; Balogun, H.A.; Sambudi, N.S.; Bilad, M.R.; Adeyemi, I.; Chakraborty, S.; Curcio, S. Recent Advances in Advanced Oxidation Processes for Removal of Contaminants from Water: A Comprehensive Review. *Process Saf. Environ. Prot.* **2021**, *146*, 220–256. [[CrossRef](#)]
13. Sgroi, M.; Snyder, S.; Roccaro, P. Comparison of AOPs at Pilot Scale: Energy Costs for Micro-Pollutants Oxidation, Disinfection by-Products Formation and Pathogens Inactivation. *Chemosphere* **2021**, *273*, 128527. [[CrossRef](#)]
14. Khan, J.A.; Sayed, M.; Khan, S.; Shah, N.S.; Dionysiou, D.D.; Boczka, G. Advanced Oxidation Processes for the Treatment of Contaminants of Emerging Concern. In *Contaminants of Emerging Concern in Water and Wastewater: Advanced Treatment Processes*; Elsevier Inc.: Cambridge, MA, USA, 2019; pp. 299–365, ISBN 9780128135617.
15. Itzel, F.; Gehrman, L.; Bielak, H.; Ebersbach, P.; Boergers, A.; Herbst, H.; Maus, C.; Simon, A.; Dopp, E.; Hammers-Wirtz, M.; et al. Investigation of Full-Scale Ozonation at a Municipal Wastewater Treatment Plant Using a Toxicity-Based Evaluation Concept. *J. Toxicol. Environ. Health—Part A Curr. Issues* **2017**, *80*, 1242–1258. [[CrossRef](#)] [[PubMed](#)]
16. Irani, R.; Khoshfetrat, A.B.; Forouzes, M. Real Municipal Wastewater Treatment Using Simultaneous Pre and Post-Ozonation Combined Biological Attached Growth Reactor: Energy Consumption Assessment. *J. Environ. Chem. Eng.* **2021**, *9*, 104595. [[CrossRef](#)]
17. Gulde, R.; Rutsch, M.; Clerc, B.; Schollée, J.E.; von Gunten, U.; McArdell, C.S. Formation of Transformation Products during Ozonation of Secondary Wastewater Effluent and Their Fate in Post-Treatment: From Laboratory- to Full-Scale. *Water Res.* **2021**, *200*, 117200. [[CrossRef](#)]
18. Fernandes, E.; Contreras, S.; Medina, F.; Martins, R.C.; Gomes, J. N-Doped Titanium Dioxide for Mixture of Parabens Degradation Based on Ozone Action and Toxicity Evaluation: Precursor of Nitrogen and Titanium Effect. *Process Saf. Environ. Prot.* **2020**, *138*, 80–89. [[CrossRef](#)]
19. Sgroi, M.; Anumol, T.; Vagliasindi, F.G.A.; Snyder, S.A.; Roccaro, P. Comparison of the New Cl₂/O₃/UV Process with Different Ozone- and UV-Based AOPs for Wastewater Treatment at Pilot Scale: Removal of Pharmaceuticals and Changes in Fluorescing Organic Matter. *Sci. Total Environ.* **2021**, *765*, 142720. [[CrossRef](#)] [[PubMed](#)]
20. Cai, Q.Q.; Jothinathan, L.; Deng, S.H.; Ong, S.L.; Ng, H.Y.; Hu, J.Y. *Fenton- and Ozone-Based AOP Processes for Industrial Effluent Treatment*; Elsevier: Amsterdam, The Netherlands, 2021; ISBN 9780128210116.
21. Fernandes, E.; Martins, R.C.; Gomes, J. Photocatalytic Ozonation of Parabens Mixture Using 10% N-TiO₂ and the Effect of Water Matrix. *Sci. Total Environ.* **2020**, *718*, 137321. [[CrossRef](#)] [[PubMed](#)]
22. Dong, P.; Xi, X.; Hou, G. Typical Non-TiO₂-Based Visible-Light Photocatalysts. In *Semiconductor Photocatalysis—Materials, Mechanisms and Applications*; BoD—Books on Demand: Norderstedt, Germany, 2016; pp. 209–229.
23. Barakat, M.A.; Kumar, R. *Photocatalytic Activity Enhancement of Titanium Dioxide Nanoparticles*; Springer: Cham, Switzerland, 2016; ISBN 9783319242699.
24. Gomes, J.; Roccamante, M.; Contreras, S.; Medina, F.; Oller, I.; Martins, R.C. Scale-up Impact over Solar Photocatalytic Ozonation with Benchmark-P25 and N-TiO₂ for Insecticides Abatement in Water. *J. Environ. Chem. Eng.* **2021**, *9*, 104915. [[CrossRef](#)]
25. Huang, F.; Yan, A.; Zhao, H. Influences of Doping on Photocatalytic Properties of TiO₂ Photocatalyst. In *Semiconductor Photocatalysis: Materials, Mechanisms and Applications*; InTech: Osaka, Japan, 2016; pp. 31–80.
26. García-López, E.I.; Palmisano, L. (Eds.) *Material Science in Photocatalysis*; Elsevier: Amsterdam, The Netherlands, 2021; ISBN 9781119130536.
27. Nguyen, T.K.A.; Pham, T.T.; Nguyen-Phu, H.; Shin, E.W. The Effect of Graphitic Carbon Nitride Precursors on the Photocatalytic Dye Degradation of Water-Dispersible Graphitic Carbon Nitride Photocatalysts. *Appl. Surf. Sci.* **2021**, *537*, 148027. [[CrossRef](#)]
28. Fernandes, R.A.; Sampaio, M.J.; Dražić, G.; Faria, J.L.; Silva, C.G. Efficient Removal of Parabens from Real Water Matrices by a Metal-Free Carbon Nitride Photocatalyst. *Sci. Total Environ.* **2020**, *716*, 135346. [[CrossRef](#)] [[PubMed](#)]
29. Orge, C.A.; Sampaio, M.J.; Faria, J.L.; Pereira, M.F.R.; Silva, C.G. Efficiency and Stability of Metal-Free Carbon Nitride in the Photocatalytic Ozonation of Oxamic Acid under Visible Light. *J. Environ. Chem. Eng.* **2020**, *8*, 104172. [[CrossRef](#)]
30. Liu, H.; Ma, S.; Shao, L.; Liu, H.; Gao, Q.; Li, B.; Fu, H.; Fu, S.; Ye, H.; Zhao, F.; et al. Defective Engineering in Graphitic Carbon Nitride Nanosheet for Efficient Photocatalytic Pathogenic Bacteria Disinfection. *Appl. Catal. B Environ.* **2020**, *261*, 118201. [[CrossRef](#)]
31. Li, Y.; Zhang, C.; Shuai, D.; Naraginti, S.; Wang, D.; Zhang, W. Visible-Light-Driven Photocatalytic Inactivation of MS2 by Metal-Free g-C₃N₄: Virucidal Performance and Mechanism. *Water Res.* **2016**, *106*, 249–258. [[CrossRef](#)] [[PubMed](#)]

32. Nagy, D.; Nagy, D.; Szilágyi, I.M.; Fan, X. Effect of the Morphology and Phases of WO₃ Nanocrystals on Their Photocatalytic Efficiency. *RSC Adv.* **2016**, *6*, 33743–33754. [[CrossRef](#)]
33. Palanisamy, G.; Bhuvanewari, K.; Pazhanivel, T.; Bharathi, G. Enriched Photocatalytic Activity of Rhodamine B Dye from Aqueous Solution Using Hollow Sphere Tungsten Trioxide Nanoparticles. *Optik* **2020**, *204*, 164171. [[CrossRef](#)]
34. Mena, E.; Rey, A.; Contreras, S.; Beltrán, F.J. Visible Light Photocatalytic Ozonation of DEET in the Presence of Different Forms of WO₃. *Catal. Today* **2015**, *252*, 100–106. [[CrossRef](#)]
35. Razali, N.A.M.; Salleh, W.N.W.; Rosman, N.; Ismail, N.H.; Ahmad, S.Z.N.; Aziz, F.; Jye, L.W.; Ismail, A.F. Palm Oil Mill Effluent Treatment Using Tungsten Trioxide: Adsorption and Photocatalytic Degradation. *Mater. Today Proc.* **2021**, *42*, 22–27. [[CrossRef](#)]
36. Basavarajappa, P.S.; Patil, S.B.; Ganganagappa, N.; Reddy, K.R.; Raghu, A.V.; Reddy, C.V. Recent Progress in Metal-Doped TiO₂, Non-Metal Doped/Codoped TiO₂ and TiO₂ Nanostructured Hybrids for Enhanced Photocatalysis. *Int. J. Hydrogen Energy* **2020**, *45*, 7764–7778. [[CrossRef](#)]
37. Varma, K.S.; Tayade, R.J.; Shah, K.J.; Joshi, P.A.; Shukla, A.D.; Gandhi, V.G. Photocatalytic Degradation of Pharmaceutical and Pesticide Compounds (PPCs) Using Doped TiO₂ Nanomaterials: A Review. *Water-Energy Nexus* **2020**, *3*, 46–61. [[CrossRef](#)]
38. Karuppasamy, P.; Ramzan Nilofar Nisha, N.; Pugazhendhi, A.; Kandasamy, S.; Pitchaimuthu, S. An Investigation of Transition Metal Doped TiO₂ photocatalysts for the Enhanced Photocatalytic Decoloration of Methylene Blue Dye under Visible Light Irradiation. *J. Environ. Chem. Eng.* **2021**, *9*, 105254. [[CrossRef](#)]
39. Lee, H.; Jang, H.S.; Kim, N.Y.; Joo, J.B. Cu-Doped TiO₂ Hollow Nanostructures for the Enhanced Photocatalysis under Visible Light Conditions. *J. Ind. Eng. Chem.* **2021**, *99*, 352–363. [[CrossRef](#)]
40. Moreira, A.J.; Malafatti, J.O.D.; Giralaldi, T.R.; Paris, E.C.; Pereira, E.C.; de Mendonça, V.R.; Mastelaro, V.R.; Freschi, G.P.G. Prozac® Photodegradation Mediated by Mn-Doped TiO₂ Nanoparticles: Evaluation of by-Products and Mechanisms Proposal. *J. Environ. Chem. Eng.* **2020**, *8*, 104543. [[CrossRef](#)]
41. Ellouzi, I.; Bouddouch, A.; Bakiz, B.; Benlhachemi, A.; Abou Oualid, H. Glucose-Assisted Ball Milling Preparation of Silver-Doped Biphasic TiO₂ for Efficient Photodegradation of Rhodamine B: Effect of Silver-Dopant Loading. *Chem. Phys. Lett.* **2021**, *770*, 138456. [[CrossRef](#)]
42. Wu, M.C.; Lin, T.H.; Hsu, K.H.; Hsu, J.F. Photo-Induced Disinfection Property and Photocatalytic Activity Based on the Synergistic Catalytic Technique of Ag Doped TiO₂ Nanofibers. *Appl. Surf. Sci.* **2019**, *484*, 326–334. [[CrossRef](#)]
43. Saber, N.B.; Mezni, A.; Alrooqi, A.; Altalhi, T. Fabrication of Efficient Au@TiO₂/RGO Heterojunction Nanocomposite: Boosted Photocatalytic Activity under Ultraviolet and Visible Light Irradiation. *J. Mater. Res. Technol.* **2021**, *12*, 2238–2246. [[CrossRef](#)]
44. Manasa, M.; Chandewar, P.R.; Mahalingam, H. Photocatalytic Degradation of Ciprofloxacin & Norfloxacin and Disinfection Studies under Solar Light Using Boron & Cerium Doped TiO₂ Catalysts Synthesized by Green EDTA-Citrate Method. *Catal. Today* **2021**, *375*, 522–536. [[CrossRef](#)]
45. Komaraiah, D.; Radha, E.; Sivakumar, J.; Reddy, M.V.R.; Sayanna, R. Influence of Fe³⁺ Ion Doping on the Luminescence Emission Behavior and Photocatalytic Activity of Fe³⁺, Eu³⁺-Codoped TiO₂ Thin Films. *J. Alloys Compd.* **2021**, *868*, 159109. [[CrossRef](#)]
46. Mancuso, A.; Sacco, O.; Vaiano, V.; Sannino, D.; Pragliola, S.; Venditto, V.; Morante, N. Visible Light Active Fe-Pr Co-Doped TiO₂ for Water Pollutants Degradation. *Catal. Today* **2021**. [[CrossRef](#)]
47. Crişan, M.; Răileanu, M.; Drăgan, N.; Crişan, D.; Ianculescu, A.; Niţoi, I.; Oancea, P.; Şomărescu, S.; Stănică, N.; Vasile, B.; et al. Sol-Gel Iron-Doped TiO₂ Nanopowders with Photocatalytic Activity. *Appl. Catal. A Gen.* **2015**, *504*, 130–142. [[CrossRef](#)]
48. Pascariu, P.; Cojocaru, C.; Homocianu, M.; Samoila, P.; Dascalu, A.; Sucheana, M. New La³⁺ Doped TiO₂ Nanofibers for Photocatalytic Degradation of Organic Pollutants: Effects of Thermal Treatment and Doping Loadings. *Ceram. Int.* **2022**, *48*, 4953–4964. [[CrossRef](#)]
49. Hernández-Ramírez, A.; Medina-Ramírez, I.; Bustos, E.; Manríquez, J.; Peralta-Hernández, J.M. *Photocatalytic Semiconductors*; Springer: Berlin/Heidelberg, Germany, 2015; ISBN 9783319109985.
50. Coronado, J.M.; Fresno, F.; Hernández-Alonso, M.D.; Portela, R. *Design of Advanced Photocatalytic Materials for Energy and Environmental Applications*; Springer: London, UK, 2013; Volume 71, ISBN 9781447150602.
51. Kayani, Z.N.; Intizar, T.; Riaz, S.; Naseem, S. Antibacterial, Magnetic and Dielectric Properties of Nano-Structured V Doped TiO₂ Thin Films Deposited by Dip Coating Technique. *Mater. Chem. Phys.* **2021**, *267*, 124659. [[CrossRef](#)]
52. Lashuk, B.; Yargeau, V. A Review of Ecotoxicity Reduction in Contaminated Waters by Heterogeneous Photocatalytic Ozonation. *Sci. Total Environ.* **2021**, *787*, 147645. [[CrossRef](#)]
53. Asgari, E.; Sheikhmohammadi, A.; Nourmoradi, H.; Nazari, S.; Aghanaghad, M. Degradation of Ciprofloxacin by Photocatalytic Ozonation Process under Irradiation with UVA: Comparative Study, Performance and Mechanism. *Process Saf. Environ. Prot.* **2021**, *147*, 356–366. [[CrossRef](#)]
54. Mecha, A.C.; Onyango, M.S.; Ochieng, A.; Momba, M.N.B. Ultraviolet and Solar Photocatalytic Ozonation of Municipal Wastewater: Catalyst Reuse, Energy Requirements and Toxicity Assessment. *Chemosphere* **2017**, *186*, 669–676. [[CrossRef](#)] [[PubMed](#)]
55. Ribeiro, A.R.; Umbuzeiro, G. de A. Effects of a Textile Azo Dye on Mortality, Regeneration, and Reproductive Performance of the Planarian, *Girardia tigrina*. *Environ. Sci. Eur.* **2014**, *26*, 1–8. [[CrossRef](#)]
56. Gomes, J.F.; Leal, I.; Bednarczyk, K.; Gmurek, M.; Stelmachowski, M.; Diak, M.; Emília Quinta-Ferreira, M.; Costa, R.; Quinta-Ferreira, R.M.; Martins, R.C. Photocatalytic Ozonation Using Doped TiO₂ Catalysts for the Removal of Parabens in Water. *Sci. Total Environ.* **2017**, *609*, 329–340. [[CrossRef](#)] [[PubMed](#)]

57. Prakash, J.; Samriti, Kumar, A.; Dai, H.; Janegitz, B.C.; Krishnan, V.; Swart, H.C.; Sun, S. Novel Rare Earth Metal-Doped One-Dimensional TiO₂ Nanostructures: Fundamentals and Multifunctional Applications. *Mater. Today Sustain.* **2021**, *13*, 100066. [[CrossRef](#)]
58. Cerrato, E.; Gaggero, E.; Calza, P.; Paganini, M.C. The Role of Cerium, Europium and Erbium Doped TiO₂ Photocatalysts in Water Treatment: A Mini-Review. *Chem. Eng. J. Adv.* **2022**, *10*, 100268. [[CrossRef](#)]
59. Mancuso, A.; Sacco, O.; Sannino, D.; Pragliola, S.; Vaiano, V. Enhanced Visible-Light-Driven Photodegradation of Acid Orange 7 Azo Dye in Aqueous Solution Using Fe-N Co-Doped TiO₂. *Arab. J. Chem.* **2020**, *13*, 8347–8360. [[CrossRef](#)]
60. Lin, L.; Wang, H.; Luo, H.; Xu, P. Enhanced Photocatalysis Using Side-Glowing Optical Fibers Coated with Fe-Doped TiO₂ Nanocomposite Thin Films. *J. Photochem. Photobiol. A Chem.* **2015**, *307–308*, 88–98. [[CrossRef](#)]
61. Gusain, R.; Kumar, N.; Ray, S.S. Factors Influencing the Photocatalytic Activity of Photocatalysts in Wastewater Treatment. In *Photocatalysts in Advanced Oxidation Processes for Wastewater Treatment*; John Wiley & Sons: Hoboken, NJ, USA, 2020; pp. 229–270.
62. Mirzaei, A.; Eddah, M.; Roualdes, S.; Ma, D.; Chaker, M. Multiple-Homojunction Gradient Nitrogen Doped TiO₂ for Photocatalytic Degradation of Sulfamethoxazole, Degradation Mechanism, and Toxicity Assessment. *Chem. Eng. J.* **2021**, *422*, 130507. [[CrossRef](#)]
63. Ramezanisani, S.; Rajabi, M.; Mohseni, F. Influence of Nitrogen Doping on Visible Light Photocatalytic Activity of TiO₂ Nanowires with Anatase-Rutile Junction. *Chem. Phys. Lett.* **2020**, *744*, 137217. [[CrossRef](#)]
64. Suwannaruang, T.; Kamonsuangkasem, K.; Kidkhunthod, P.; Chirawatkul, P.; Saiyasombat, C.; Chanlek, N.; Wantala, K. Influence of Nitrogen Content Levels on Structural Properties and Photocatalytic Activities of Nanorice-like N-Doped TiO₂ with Various Calcination Temperatures. *Mater. Res. Bull.* **2018**, *105*, 265–276. [[CrossRef](#)]
65. Erdogan, N.; Bouziani, A.; Park, J.; Micusik, M.; Kim, S.Y.; Majkova, E.; Omastova, M.; Ozturk, A. Synthesis and Enhanced Photocatalytic Activity of Nitrogen-Doped Triphasic TiO₂ Nanoparticles. *J. Photochem. Photobiol. A Chem.* **2019**, *377*, 92–100. [[CrossRef](#)]
66. Toe, E.D.; Kurniawan, W.; Mariquit, E.G.; Hinode, H. Synthesis of N-Doped Mesoporous TiO₂ by Facile One-Step Solvothermal Process for Visible Light Photocatalytic Degradation of Organic Pollutant. *J. Environ. Chem. Eng.* **2018**, *6*, 5125–5134. [[CrossRef](#)]
67. Yadav, V.; Saini, V.K.; Sharma, H. How Different Dopants Leads to Difference in Photocatalytic Activity in Doped TiO₂? *Ceram. Int.* **2020**, *46*, 27308–27317. [[CrossRef](#)]
68. Bakre, P.V.; Tilve, S.G.; Shirsat, R.N. Influence of N Sources on the Photocatalytic Activity of N-Doped TiO₂. *Arab. J. Chem.* **2020**, *13*, 7637–7651. [[CrossRef](#)]
69. Zhao, W.; Liu, S.; Zhang, S.; Wang, R.; Wang, K. Preparation and Visible-Light Photocatalytic Activity of N-Doped TiO₂ by Plasma-Assisted Sol-Gel Method. *Catal. Today* **2019**, *337*, 37–43. [[CrossRef](#)]
70. Gao, H.; Zhou, J.; Dai, D.; Qu, Y. Photocatalytic Activity and Electronic Structure Analysis of N-Doped Anatase TiO₂: A Combined Experimental and Theoretical Study. *Chem. Eng. Technol.* **2009**, *32*, 867–872. [[CrossRef](#)]
71. Assayehgn, E.; Solaiappan, A.; Chebude, Y.; Alemayehu, E. Fabrication of Tunable Anatase/Rutile Heterojunction N/TiO₂ Nanophotocatalyst for Enhanced Visible Light Degradation Activity. *Appl. Surf. Sci.* **2020**, *515*, 145966. [[CrossRef](#)]
72. Chaturvedi, R.; Singh, P.K. Materials Today: Proceedings Synthesis and Characterization of Nano Crystalline Nitrogen Doped Titanium Dioxide. *Mater. Today Proc.* **2021**, *45*, 3666–3669. [[CrossRef](#)]
73. Wafi, A.; Szabó-Bárdos, E.; Horváth, O.; Makó, É.; Jakab, M.; Zsirka, B. Coumarin-Based Quantification of Hydroxyl Radicals and Other Reactive Species Generated on Excited Nitrogen-Doped TiO₂. *J. Photochem. Photobiol. A Chem.* **2021**, *404*, 112913. [[CrossRef](#)]
74. Huang, J.; Dou, L.; Li, J.; Zhong, J.; Li, M.; Wang, T. Excellent Visible Light Responsive Photocatalytic Behavior of N-Doped TiO₂ toward Decontamination of Organic Pollutants. *J. Hazard. Mater.* **2021**, *403*, 123857. [[CrossRef](#)]
75. Zhang, J.; Xie, M.; Zhao, H.; Zhang, L.R.; Wei, G.; Zhao, G. Preferential and Efficient Degradation of Phenolic Pollutants with Cooperative Hydrogen-Bond Interactions in Photocatalytic Process. *Chemosphere* **2021**, *269*, 129404. [[CrossRef](#)]
76. Ravidhas, C.; Anitha, B.; Venkatesh, R.; Monica, S.E.S.; Gopalakrishna, D.; Raj, A.M.E.; Ravichandran, K. Role of Fluorine Doping on Luminescence Centers and Enhanced Photocatalytic Performance of Nebulizer Sprayed TiO₂ Films under Visible Light. *J. Lumin.* **2018**, *198*, 272–283. [[CrossRef](#)]
77. Hwang, J.; Kalanur, S.S.; Seo, H. Identification of Visible Photocatalytic and Photoelectrochemical Properties of I-TiO₂ via Electronic Band Structure. *Electrochim. Acta* **2017**, *252*, 482–489. [[CrossRef](#)]
78. Zhou, L.; Cai, M.; Zhang, X.; Cui, N.; Chen, G.; Zou, G. In-Situ Nitrogen-Doped Black TiO₂ with Enhanced Visible-Light-Driven Photocatalytic Inactivation of Microcystis Aeruginosa Cells: Synthesis, Performance and Mechanism. *Appl. Catal. B Environ.* **2020**, *272*, 119019. [[CrossRef](#)]
79. Tzeng, J.H.; Weng, C.H.; Yen, L.T.; Gaybullaev, G.; Chang, C.J.; de Luna, M.D.G.; Lin, Y.T. Inactivation of Pathogens by Visible Light Photocatalysis with Nitrogen-Doped TiO₂ and Tourmaline-Nitrogen Co-Doped TiO₂. *Sep. Purif. Technol.* **2021**, *274*, 118979. [[CrossRef](#)]
80. Boningari, T.; Inturi, S.N.R.; Suidan, M.; Smirniotis, P.G. Novel One-Step Synthesis of Sulfur Doped-TiO₂ by Flame Spray Pyrolysis for Visible Light Photocatalytic Degradation of Acetaldehyde. *Chem. Eng. J.* **2018**, *339*, 249–258. [[CrossRef](#)]
81. Bento, R.T.; Correa, O.V.; Pillis, M.F. Photocatalytic Activity of Undoped and Sulfur-Doped TiO₂ Films Grown by MOCVD for Water Treatment under Visible Light. *J. Eur. Ceram. Soc.* **2019**, *39*, 3498–3504. [[CrossRef](#)]
82. Portela, R. Non-Metal Doping for Band-Gap Engineering Raquel. In *Design of Advanced Photocatalytic Materials for Energy and Environmental Applications*. In *Green Energy and Technology*; Coronado, J.M., Fresno, F., Hernández-Alonso, M.D., Portela, R., Eds.; Springer: London, UK, 2013; Volume 71, pp. 287–309, ISBN 9781447150602.

83. He, J.; Kumar, A.; Khan, M.; Lo, I.M.C. Critical Review of Photocatalytic Disinfection of Bacteria: From Noble Metals- and Carbon Nanomaterials-TiO₂ Composites to Challenges of Water Characteristics and Strategic Solutions. *Sci. Total Environ.* **2021**, *758*, 143953. [[CrossRef](#)] [[PubMed](#)]
84. Wang, Y.; Wu, Y.; Yang, H.; Xue, X.; Liu, Z. Doping TiO₂ with Boron or/and Cerium Elements: Effects on Photocatalytic Antimicrobial Activity. *Vacuum* **2016**, *131*, 58–64. [[CrossRef](#)]
85. Jahdi, M.; Mishra, S.B.; Nxumalo, E.N.; Mhlanga, S.D.; Mishra, A.K. Smart Pathways for the Photocatalytic Degradation of Sulfamethoxazole Drug Using F-Pd Co-Doped TiO₂ Nanocomposites. *Appl. Catal. B Environ.* **2020**, *267*, 118716. [[CrossRef](#)]
86. Khedr, T.M.; El-Sheikh, S.M.; Hakki, A.; Ismail, A.A.; Badawy, W.A.; Bahnemann, D.W. Highly Active Non-Metals Doped Mixed-Phase TiO₂ for Photocatalytic Oxidation of Ibuprofen under Visible Light. *J. Photochem. Photobiol. A Chem.* **2017**, *346*, 530–540. [[CrossRef](#)]
87. Venkatesan, A.; Al-onazi, W.A.; Elshikh, M.S.; Pham, T.H.; Suganya, S.; Boobas, S.; Priyadharsan, A. Study of Synergistic Effect of Cobalt and Carbon Codoped with TiO₂ Photocatalyst for Visible Light Induced Degradation of Phenol. *Chemosphere* **2022**, *305*, 135333. [[CrossRef](#)]
88. Ariza-Tarazona, M.C.; Villarreal-Chiu, J.F.; Hernández-López, J.M.; Rivera De la Rosa, J.; Barbieri, V.; Siligardi, C.; Cedillo-González, E.I. Microplastic Pollution Reduction by a Carbon and Nitrogen-Doped TiO₂: Effect of PH and Temperature in the Photocatalytic Degradation Process. *J. Hazard. Mater.* **2020**, *395*, 122632. [[CrossRef](#)]
89. Thongpool, V.; Phunpueok, A.; Jaiyen, S.; Sornkwan, T. Results in Physics Synthesis and Photocatalytic Activity of Copper and Nitrogen Co-Doped Titanium Dioxide Nanoparticles. *Results Phys.* **2020**, *16*, 102948. [[CrossRef](#)]
90. Wu, Y.; Dong, Y.; Xia, X.; Liu, X.; Li, H. Facile Synthesis of N-F Codoped and Molecularly Imprinted TiO₂ for Enhancing Photocatalytic Degradation of Target Contaminants. *Appl. Surf. Sci.* **2016**, *364*, 829–836. [[CrossRef](#)]
91. Razali, N.A.M.; Salleh, W.N.W.; Aziz, F.; Jye, L.W.; Yusof, N.; Ismail, A.F. Review on Tungsten Trioxide as a Photocatalysts for Degradation of Recalcitrant Pollutants. *J. Clean. Prod.* **2021**, *309*, 127438. [[CrossRef](#)]
92. Palharim, P.H.; Fusari, B.L.D.d.R.; Ramos, B.; Otubo, L.; Teixeira, A.C.S.C. Effect of HCl and HNO₃ on the Synthesis of Pure and Silver-Based WO₃ for Improved Photocatalytic Activity under Sunlight. *J. Photochem. Photobiol. A Chem.* **2022**, *422*, 113550. [[CrossRef](#)]
93. Hanif, M.A.; Akter, J.; Islam, M.A.; Sapkota, K.P.; Hahn, J.R. Visible-Light-Driven Enhanced Photocatalytic Performance Using Cadmium-Doping of Tungsten (VI) Oxide and Nanocomposite Formation with Graphitic Carbon Nitride Disks. *Appl. Surf. Sci.* **2021**, *565*, 150541. [[CrossRef](#)]
94. Mehmood, F.; Iqbal, J.; Jan, T.; Gul, A.; Mansoor, Q.; Faryal, R. Structural, Photoluminescence, Electrical, Anti Cancer and Visible Light Driven Photocatalytic Characteristics of Co Doped WO₃ Nanoplates. *Vib. Spectrosc.* **2017**, *93*, 78–89. [[CrossRef](#)]
95. Quyen, V.T.; Kim, J.T.; Park, P.M.; Huong, P.T.; Viet, N.M.; Thang, P.Q. Enhanced the Visible Light Photocatalytic Decomposition of Antibiotic Pollutant in Wastewater by Using Cu Doped WO₃. *J. Environ. Chem. Eng.* **2021**, *9*, 104737. [[CrossRef](#)]
96. Luxmi, V.; Kumar, A. Enhanced Photocatalytic Performance of m-WO₃ and m-Fe-Doped WO₃ Cuboids Synthesized via Sol-Gel Approach Using Egg Albumen as a Solvent. *Mater. Sci. Semicond. Process.* **2019**, *104*, 104690. [[CrossRef](#)]
97. Govindaraj, T.; Mahendran, C.; Marnadu, R.; Shkir, M.; Manikandan, V.S. The Remarkably Enhanced Visible-Light-Photocatalytic Activity of Hydrothermally Synthesized WO₃ Nanorods: An Effect of Gd Doping. *Ceram. Int.* **2021**, *47*, 4267–4278. [[CrossRef](#)]
98. Yazdanbakhsh, A.R.; Eslami, A.; Massoudinejad, M.; Avazpour, M. Enhanced Degradation of Sulfamethoxazole Antibiotic from Aqueous Solution Using Mn-WO₃/LED Photocatalytic Process: Kinetic, Mechanism, Degradation Pathway and Toxicity Reduction. *Chem. Eng. J.* **2020**, *380*, 122497. [[CrossRef](#)]
99. Zheng, Y.; Chen, G.; Yu, Y.; Zhou, Y.; He, F. Synthesis of Carbon Doped WO₃·0.33H₂O Hierarchical Photocatalyst with Improved Photocatalytic Activity. *Appl. Surf. Sci.* **2016**, *362*, 182–190. [[CrossRef](#)]
100. Tijani, J.O.; Ugochukwu, O.; Fadipe, L.A.; Bankole, M.T.; Abdulkareem, A.S.; Roos, W.D. Photocatalytic Degradation of Local Dyeing Wastewater by Iodine-Phosphorus Co-Doped Tungsten Trioxide Nanocomposites under Natural Sunlight Irradiation. *J. Environ. Manag.* **2019**, *236*, 519–533. [[CrossRef](#)]
101. Han, F.; Li, H.; Fu, L.; Yang, J.; Liu, Z. Synthesis of S-Doped WO₃ Nanowires with Enhanced Photocatalytic Performance towards Dye Degradation. *Chem. Phys. Lett.* **2016**, *651*, 183–187. [[CrossRef](#)]
102. Tahir, M.B.; Sagir, M. Carbon Nanodots and Rare Metals (RM = La, Gd, Er) Doped Tungsten Oxide Nanostructures for Photocatalytic Dyes Degradation and Hydrogen Production. *Sep. Purif. Technol.* **2019**, *209*, 94–102. [[CrossRef](#)]
103. Ma, T.; Shen, Q.; Xue, B.Z.J.; Guan, R.; Liu, X.; Jia, H.; Xu, B. Facile Synthesis of Fe-Doped g-C₃N₄ for Enhanced Visible-Light Photocatalytic Activity. *Inorg. Chem. Commun.* **2019**, *107*, 107451. [[CrossRef](#)]
104. Pham, T.H.; Park, J.W.; Kim, T.Y. Enhanced Photodegradation of Paracetamol from Water by Cobalt Doped Graphitic Carbon Nitride. *Sol. Energy* **2021**, *215*, 151–156. [[CrossRef](#)]
105. Pham, T.H.; Jung, S.H.; Kim, T.Y. Enhanced Photodegradation of Toxic Volatile Organic Pollutants Using Ni-Doped Graphitic Carbon Nitride under Natural Solar Light. *Sol. Energy* **2021**, *224*, 18–26. [[CrossRef](#)]
106. Tripathi, A.; Narayanan, S. Potassium Doped Graphitic Carbon Nitride with Extended Optical Absorbance for Solar Light Driven Photocatalysis. *Appl. Surf. Sci.* **2019**, *479*, 1–11. [[CrossRef](#)]
107. Tri, N.L.M.; Kim, J.; Giang, B.L.; Tahtamouni, T.M.A.; Huong, P.T.; Lee, C.; Viet, N.M.; Trung, D.Q. Ag-Doped Graphitic Carbon Nitride Photocatalyst with Remarkably Enhanced Photocatalytic Activity towards Antibiotic in Hospital Wastewater under Solar Light. *J. Ind. Eng. Chem.* **2019**, *80*, 597–605. [[CrossRef](#)]

108. Bawazeer, T.M.; Al-Shehri, B.M.; Alsoufi, M.S.; Shkir, M.; Hamdy, M.S. Solvent-Free Facile Fabrication of Gold Nanoparticles Loaded Carbon Nitride and Their Photocatalytic Performance under Visible Light Illumination. *Optik* **2021**, *241*, 167205. [[CrossRef](#)]
109. Li, G.; Wang, B.; Zhang, J.; Wang, R.; Liu, H. Er-Doped g-C₃N₄ for Photodegradation of Tetracycline and Tylosin: High Photocatalytic Activity and Low Leaching Toxicity. *Chem. Eng. J.* **2020**, *391*, 123500. [[CrossRef](#)]
110. Viet, N.M.; Trung, D.Q.; Giang, B.L.; Tri, N.L.M.; Thao, P.; Pham, T.H.; Kamand, F.Z.; Al Tahtamouni, T.M. Noble Metal -Doped Graphitic Carbon Nitride Photocatalyst for Enhancement Photocatalytic Decomposition of Antibiotic Pollutant in Wastewater under Visible Light. *J. Water Process Eng.* **2019**, *32*, 100954. [[CrossRef](#)]
111. Xu, J.; Brenner, T.J.K.; Chen, Z.; Neher, D.; Antonietti, M.; Shalom, M. Upconversion-Agent Induced Improvement of g-C₃N₄ Photocatalyst under Visible Light. *ACS Appl. Mater. Interfaces* **2014**, *6*, 16481–16486. [[CrossRef](#)]
112. Xiong, T.; Cen, W.; Zhang, Y.; Dong, F. Bridging the g-C₃N₄ Interlayers for Enhanced Photocatalysis. *ACS Catal.* **2016**, *6*, 2462–2472. [[CrossRef](#)]
113. Liu, J.; Liang, H.; Li, C.; Bai, J. Construction of V-Doped Graphitic Carbon Nitride with Nanotube Structure for Sustainable Photodegradation of Tetracycline. *Vacuum* **2022**, *204*, 111342. [[CrossRef](#)]
114. Zhang, B.; Li, X.; Zhao, Y.; Song, H.; Wang, H. Facile Synthesis of Oxygen Doped Mesoporous Graphitic Carbon Nitride with High Photocatalytic Degradation Efficiency under Simulated Solar Irradiation. *Colloids Surfaces A Physicochem. Eng. Asp.* **2019**, *580*, 123736. [[CrossRef](#)]
115. Praus, P.; Smýkalová, A.; Foniok, K.; Novák, V.; Hrbáč, J. Doping of Graphitic Carbon Nitride with Oxygen by Means of Cyanuric Acid: Properties and Photocatalytic Applications. *J. Environ. Chem. Eng.* **2021**, *9*, 105498. [[CrossRef](#)]
116. Krumova, K.; Cosa, G.; Aubry, J.; Kanofsky, J.R. Overview of Reactive Oxygen Species Katerina. In *Singlet Oxygen: Applications in Biosciences and Nanosciences*; The Royal Society of Chemistry: Cambridge, UK, 2016; pp. 3–18, ISBN 9781412916837.
117. Wang, S.; He, F.; Zhao, X.; Zhang, J.; Ao, Z.; Wu, H.; Yin, Y.; Shi, L.; Xu, X.; Zhao, C.; et al. Phosphorous Doped Carbon Nitride Nanobelts for Photodegradation of Emerging Contaminants and Hydrogen Evolution. *Appl. Catal. B Environ.* **2019**, *257*, 117931. [[CrossRef](#)]
118. Liang, Z.; Ba, G.; Li, H.; Du, N.; Hou, W. Facile Synthesis of Silicon-Doped Polymeric Carbon Nitride with Enhanced Photocatalytic Performance. *J. Alloys Compd.* **2020**, *815*, 152488. [[CrossRef](#)]
119. Ganganboina, A.B.; Nguyen, M.D.; Nguyen, T.H.L.; Kuncoro, E.P.; Doong, R.-A. Boron and Phosphorus Co-Doped One-Dimensional Graphitic Carbon Nitride for Enhanced Visible-Light-Driven Photodegradation of Diclofenac. *Chem. Eng. J.* **2021**, *425*, 131520. [[CrossRef](#)]
120. Cao, M.; Wang, K.; Tudela, I.; Fan, X. Improve Photocatalytic Performance of g-C₃N₄ through Balancing the Interstitial and Substitutional Chlorine Doping. *Appl. Surf. Sci.* **2021**, *536*, 147784. [[CrossRef](#)]
121. Yi, F.; Gan, H.; Jin, H.; Zhao, W.; Zhang, K.; Jin, H.; Zhang, H.; Qian, Y.; Ma, J. Sulfur- and Chlorine-Co-Doped g-C₃N₄ Nanosheets with Enhanced Active Species Generation for Boosting Visible-Light Photodegradation Activity. *Sep. Purif. Technol.* **2020**, *233*, 115997. [[CrossRef](#)]
122. Wang, Y.; Zhou, J.; Wang, F.; Xie, Y.; Liu, S.; Ao, Z.; Li, C. Hydrogen Generation from Photocatalytic Treatment of Wastewater Containing Pharmaceuticals and Personal Care Products by Oxygen-Doped Crystalline Carbon Nitride. *Sep. Purif. Technol.* **2022**, *296*, 121425. [[CrossRef](#)]
123. Liu, X.; Zhou, Y.; Ma, Y.; Fang, S.; Kong, F.; Pang, X. Photocatalytic Degradation of Dinotefuran by Layered Phosphorus-Doped Carbon Nitride and Its Mechanism. *J. Photochem. Photobiol. A Chem.* **2021**, *414*, 113287. [[CrossRef](#)]
124. Pandit, B.B.; Sonawane, S.; Aniruddha, V.P. (Eds.) *Handbook of Nanomaterials for Wastewater Treatment: Fundamental and Scale Up Issues*, 1st ed.; Elsevier: Amsterdam, The Netherlands, 2021; ISBN 9789896540821.
125. Khan, M.M.; Pradhan, D.; Sohn, Y. (Eds.) *Nanocomposites for Visible Light-Induced Photocatalysis*; Springer: Berlin/Heidelberg, Germany, 2017; ISBN 9783319624457.
126. Mugunthan, E.; Saidutta, M.B.; Jagadeeshbabu, P.E. Visible Light Assisted Photocatalytic Degradation of Diclofenac Using TiO₂-WO₃ Mixed Oxide Catalysts. *Environ. Nanotechnol. Monit. Manag.* **2018**, *10*, 322–330. [[CrossRef](#)]
127. El-Yazeed, W.S.A.; Ahmed, A.I. Photocatalytic Activity of Mesoporous WO₃/TiO₂ Nanocomposites for the Photodegradation of Methylene Blue. *Inorg. Chem. Commun.* **2019**, *105*, 102–111. [[CrossRef](#)]
128. Wang, Q.; Zhang, W.; Hu, X.; Xu, L.; Chen, G.; Li, X. Hollow Spherical WO₃/TiO₂ Heterojunction for Enhancing Photocatalytic Performance in Visible-Light. *J. Water Process Eng.* **2021**, *40*, 101943. [[CrossRef](#)]
129. Su, X.; Liu, C.j.; Liu, Y.; Yang, Y.; Liu, X.; Chen, S. Construction of BiVO₄ Nanosheets@WO₃ Arrays Heterojunction Photoanodes by Versatile Phase Transformation Strategy. *Trans. Nonferrous Met. Soc. China* **2021**, *31*, 533–544. [[CrossRef](#)]
130. Meng, S.; Sun, W.; Zhang, S.; Zheng, X.; Fu, X.; Chen, S. Insight into the Transfer Mechanism of Photogenerated Carriers for WO₃/TiO₂ Heterojunction Photocatalysts: Is It the Transfer of Band-Band or Z-Scheme? Why? *J. Phys. Chem. C* **2018**, *122*, 26326–26336. [[CrossRef](#)]
131. Wei, Y.; Huang, Y.; Fang, Y.; Zhao, Y.; Luo, D.; Guo, Q.; Fan, L.; Wu, J. Hollow Mesoporous TiO₂/WO₃ Sphere Heterojunction with High Visible-Light-Driven Photocatalytic Activity. *Mater. Res. Bull.* **2019**, *119*, 110571. [[CrossRef](#)]
132. Zhou, Z.; Niu, X.; Zhang, Y.; Wang, J. Janus MoSSe/WSeTe Heterostructures: A Direct Z-Scheme Photocatalyst for Hydrogen Evolution. *J. Mater. Chem. A* **2019**, *7*, 21835–21842. [[CrossRef](#)]
133. Cordero-García, A.; Guzmán-Mar, J.L.; Hinojosa-Reyes, L.; Ruiz-Ruiz, E.; Hernández-Ramírez, A. Effect of Carbon Doping on WO₃/TiO₂ Coupled Oxide and Its Photocatalytic Activity on Diclofenac Degradation. *Ceram. Int.* **2016**, *42*, 9796–9803. [[CrossRef](#)]

134. Basumatary, B.; Basumatary, R.; Ramchiary, A.; Konwar, D. Evaluation of Ag@TiO₂/WO₃ Heterojunction Photocatalyst for Enhanced Photocatalytic Activity towards Methylene Blue Degradation. *Chemosphere* **2022**, *286*, 131848. [[CrossRef](#)] [[PubMed](#)]
135. Chen, C.; Liu, X.; Long, H.; Ding, F.; Liu, Q.; Chen, X. Preparation and Photocatalytic Performance of Graphene Oxide/WO₃ Quantum Dots/TiO₂@SiO₂ Microspheres. *Vacuum* **2019**, *164*, 66–71. [[CrossRef](#)]
136. Deng, M.; Cao, X.; Li, Z.; Tang, B. Hybrid Triazine-Based g-C₃N₄(001)/ Anatase TiO₂(001) Heterojunction: Insights into Enhanced Photocatalytic Mechanisms Via DFT Calculation. *J. Photochem. Photobiol. A Chem.* **2022**, *423*, 113577. [[CrossRef](#)]
137. Barzegar, M.H.; Sabzehmeidani, M.M.; Ghaedi, M.; Avargani, V.M.; Moradi, Z.; Roy, V.A.L.; Heidari, H. S-Scheme Heterojunction g-C₃N₄/TiO₂ with Enhanced Photocatalytic Activity for Degradation of a Binary Mixture of Cationic Dyes Using Solar Parabolic Trough Reactor. *Chem. Eng. Res. Des.* **2021**, *174*, 307–318. [[CrossRef](#)]
138. Gahlot, S.; Dappozze, F.; Mishra, S.; Guillard, C. High Surface Area g-C₃N₄ and g-C₃N₄-TiO₂ Photocatalytic Activity under UV and Visible Light: Impact of Individual Component. *J. Environ. Chem. Eng.* **2021**, *9*, 105587. [[CrossRef](#)]
139. Li, G.; Nie, X.; Chen, J.; Jiang, Q.; An, T.; Wong, P.K.; Zhang, H.; Zhao, H.; Yamashita, H. Enhanced Visible-Light-Driven Photocatalytic Inactivation of Escherichia Coli Using g-C₃N₄/TiO₂ Hybrid Photocatalyst Synthesized Using a Hydrothermal-Calcination Approach. *Water Res.* **2015**, *86*, 17–24. [[CrossRef](#)]
140. Liu, Y.; Zeng, X.; Hu, X.; Hu, J.; Wang, Z.; Yin, Y.; Sun, C.; Zhang, X. Two-Dimensional g-C₃N₄/TiO₂ Nanocomposites as Vertical Z-Scheme Heterojunction for Improved Photocatalytic Water Disinfection. *Catal. Today* **2019**, *335*, 243–251. [[CrossRef](#)]
141. Huang, J.; Wang, B.; Hao, Z.; Zhou, Z.; Qu, Y. Boosting Charge Separation and Broadening NIR Light Response over Defected WO₃ Quantum Dots Coupled g-C₃N₄ Nanosheets for Photocatalytic Degrading Antibiotics. *Chem. Eng. J.* **2021**, *416*, 129109. [[CrossRef](#)]
142. Cadan, F.M.; Ribeiro, C.; Azevedo, E.B. Improving g-C₃N₄:WO₃ Z-Scheme Photocatalytic Performance under Visible Light by Multivariate Optimization of g-C₃N₄ Synthesis. *Appl. Surf. Sci.* **2021**, *537*, 147904. [[CrossRef](#)]
143. Divakaran, K.; Baishnisha, A.; Balakumar, V.; Perumal, K.N.; Meenakshi, C.; Kannan, R.S. Photocatalytic Degradation of Tetracycline under Visible Light Using TiO₂@sulfur Doped Carbon Nitride Nanocomposite Synthesized via In-Situ Method. *J. Environ. Chem. Eng.* **2021**, *9*, 105560. [[CrossRef](#)]
144. Dehkordi, A.B.; Badiei, A. Insight into the Activity of TiO₂@nitrogen-Doped Hollow Carbon Spheres Supported on g-C₃N₄ for Robust Photocatalytic Performance. *Chemosphere* **2022**, *288*, 132392. [[CrossRef](#)] [[PubMed](#)]
145. Abbasi-Asl, H.; Sabzehmeidani, M.M.; Ghaedi, M. Efficient Degradation of Metronidazole Antibiotic by TiO₂/Ag₃PO₄/g-C₃N₄ Ternary Composite Photocatalyst in a Continuous Flow-Loop Photoreactor. *J. Environ. Chem. Eng.* **2021**, *9*, 105963. [[CrossRef](#)]
146. Wang, C.; Luo, S.; Liu, C.; Chen, C. WO₃ Quantum Dots Enhanced the Photocatalytic Performances of Graphene Oxide/TiO₂ Films under Flowing Dye Solution. *Inorg. Chem. Commun.* **2020**, *115*, 107875. [[CrossRef](#)]
147. Zeng, X.; Wang, Z.; Wang, G.; Gengenbach, T.R.; McCarthy, D.T.; Deletic, A.; Yu, J.; Zhang, X. Highly Dispersed TiO₂ Nanocrystals and WO₃ Nanorods on Reduced Graphene Oxide: Z-Scheme Photocatalysis System for Accelerated Photocatalytic Water Disinfection. *Appl. Catal. B Environ.* **2017**, *218*, 163–173. [[CrossRef](#)]
148. Sun, X.; He, W.; Yang, T.; Ji, H.; Liu, W.; Lei, J.; Liu, Y.; Cai, Z. Ternary TiO₂/WO₃/CQDs Nanocomposites for Enhanced Photocatalytic Mineralization of Aqueous Cephalixin: Degradation Mechanism and Toxicity Evaluation. *Chem. Eng. J.* **2021**, *412*, 128679. [[CrossRef](#)]
149. Wang, G.; Zhou, F.; Yuan, B.; Xiao, S.; Kuang, A.; Zhong, M.; Dang, S.; Long, X.; Zhang, W. Strain-Tunable Visible-Light-Responsive Photocatalytic Properties of Two-Dimensional Cds/g-C₃N₄: A Hybrid Density Functional Study. *Nanomaterials* **2019**, *9*, 244. [[CrossRef](#)] [[PubMed](#)]
150. Someswararao, M.V.; Dubey, R.S.; Subbarao, P.S.V. Electrospun Composite Nanofibers Prepared by Varying Concentrations of TiO₂/ZnO Solutions for Photocatalytic Applications. *J. Photochem. Photobiol.* **2021**, *6*, 100016. [[CrossRef](#)]
151. Das, A.; Kumar, P.M.; Bhagavathiachari, M.; Nair, R.G. Hierarchical ZnO-TiO₂ Nanoheterojunction: A Strategy Driven Approach to Boost the Photocatalytic Performance through the Synergy of Improved Surface Area and Interfacial Charge Transport. *Appl. Surf. Sci.* **2020**, *534*, 147321. [[CrossRef](#)]
152. Cipagauta-Díaz, S.; Estrella-González, A.; Navarrete-Magaña, M.; Gómez, R. N Doped-TiO₂ Coupled to BiVO₄ with High Performance in Photodegradation of Ofloxacin Antibiotic and Rhodamine B Dye under Visible Light. *Catal. Today* **2021**, *394*, 445–457. [[CrossRef](#)]
153. Sharma, S.; Kumar, N.; Mari, B.; Chauhan, N.S.; Mittal, A.; Maken, S.; Kumari, K. Solution Combustion Synthesized TiO₂/Bi₂O₃/CuO Nano-Composites and Their Photocatalytic Activity Using Visible LEDs Assisted Photoreactor. *Inorg. Chem. Commun.* **2021**, *125*, 108418. [[CrossRef](#)]
154. Chawla, H.; Chandra, A.; Ingole, P.P.; Garg, S. Recent Advancements in Enhancement of Photocatalytic Activity Using Bismuth-Based Metal Oxides Bi₂MO₆ (M = W, Mo, Cr) for Environmental Remediation and Clean Energy Production. *J. Ind. Eng. Chem.* **2021**, *95*, 1–15. [[CrossRef](#)]
155. Munguti, L.; Dejene, F. Influence of Annealing Temperature on Structural, Optical and Photocatalytic Properties of ZnO-TiO₂ Composites for Application in Dye Removal in Water. *Nano-Struct. Nano-Objects* **2020**, *24*, 100594. [[CrossRef](#)]
156. Bouziani, A.; Park, J.; Ozturk, A. Synthesis of α-Fe₂O₃/TiO₂ Heterogeneous Composites by the Sol-Gel Process and Their Photocatalytic Activity. *J. Photochem. Photobiol. A Chem.* **2020**, *400*, 112718. [[CrossRef](#)]

157. Peña-Velasco, G.; Hinojosa-Reyes, L.; Morán-Quintanilla, G.A.; Hernández-Ramírez, A.; Villanueva-Rodríguez, M.; Guzmán-Mar, J.L. Synthesis of Heterostructured Catalyst Coupling MOF Derived Fe_2O_3 with TiO_2 for Enhanced Photocatalytic Activity in Anti-Inflammatory Drugs Mixture Degradation. *Ceram. Int.* **2021**, *47*, 24632–24640. [[CrossRef](#)]
158. Li, Y.; Yang, B.; Liu, B. MOF Assisted Synthesis of $\text{TiO}_2/\text{Au}/\text{Fe}_2\text{O}_3$ Hybrids with Enhanced Photocatalytic Hydrogen Production and Simultaneous Removal of Toxic Phenolic Compounds. *J. Mol. Liq.* **2021**, *322*, 114815. [[CrossRef](#)]
159. Lu, F.; Chen, K.; Feng, Q.; Cai, H.; Ma, D.; Wang, D.; Li, X.; Zuo, C.; Wang, S. Insight into the Enhanced Magnetic Separation and Photocatalytic Activity of Sn-Doped TiO_2 Core-Shell Photocatalyst. *J. Environ. Chem. Eng.* **2021**, *9*, 105840. [[CrossRef](#)]
160. Liu, N.; Ming, J.; Sharma, A.; Sun, X.; Kawazoe, N.; Chen, G.; Yang, Y. Sustainable Photocatalytic Disinfection of Four Representative Pathogenic Bacteria Isolated from Real Water Environment by Immobilized TiO_2 -Based Composite and Its Mechanism. *Chem. Eng. J.* **2021**, *426*, 131217. [[CrossRef](#)]
161. Mohammed, M.K.A. Sol-Gel Synthesis of Au-Doped TiO_2 Supported SWCNT Nanohybrid with Visible-Light-Driven Photocatalytic for High Degradation Performance toward Methylene Blue Dye. *Optik* **2020**, *223*, 165607. [[CrossRef](#)]
162. Thomas, C.-T.; Manisekaran, R.; Santoyo-Salazar, J.; Schoefs, B.; Velumani, S.; Castaneda, H.; Jantrania, A. Graphene Oxide Decorated TiO_2 and BiVO_4 Nanocatalysts for Enhanced Visible-Light-Driven Photocatalytic Bacterial Inactivation. *J. Photochem. Photobiol. A Chem.* **2021**, *418*, 113374. [[CrossRef](#)]
163. Huang, C.; Peng, B. Photocatalytic Degradation of Patulin in Apple Juice Based on Nitrogen-Doped Chitosan- TiO_2 Nanocomposite Prepared by a New Approach. *Lwt* **2021**, *140*, 110726. [[CrossRef](#)]
164. Wang, X.; Wang, X.; Zhao, J.; Song, J.; Wang, J.; Ma, R.; Ma, J. Solar Light-Driven Photocatalytic Destruction of Cyanobacteria by F-Ce- TiO_2 /Expanded Perlite Floating Composites. *Chem. Eng. J.* **2017**, *320*, 253–263. [[CrossRef](#)]
165. Asadi, A.M.S.; Malakootian, M.; Kowsari, E.; Alidadi, H. Ionic Liquid-Assisted Sol-Gel Synthesis of Fe_2O_3 - TiO_2 for Enhanced Photocatalytic Degradation of Bisphenol a under UV Illumination: Modeling and Optimization Using Response Surface Methodology. *Optik* **2020**, *204*, 164229. [[CrossRef](#)]
166. Orge, C.A.; Soares, O.S.G.P.; Faria, J.L.; Pereira, M.F.R. Synthesis of TiO_2 -Carbon Nanotubes through Ball-Milling Method for Mineralization of Oxamic Acid (OMA) by Photocatalytic Ozonation. *J. Environ. Chem. Eng.* **2017**, *5*, 5599–5607. [[CrossRef](#)]
167. Chávez, A.M.; Quiñones, D.H.; Rey, A.; Beltrán, F.J.; Álvarez, P.M. Simulated Solar Photocatalytic Ozonation of Contaminants of Emerging Concern and Effluent Organic Matter in Secondary Effluents by a Reusable Magnetic Catalyst. *Chem. Eng. J.* **2020**, *398*, 125642. [[CrossRef](#)]
168. Asgari, E.; Farzadkia, M.; Esrafil, A.; Badi, M.Y.; Jokandan, S.F.; Sobhi, H.R. Application of a Photocatalytic Ozonation Process Using TiO_2 Magnetic Nanoparticles for the Removal of Ceftazide from Aqueous Solutions: Evaluation of Performance, Comparative Study and Mechanism. *Optik* **2020**, *212*, 164667. [[CrossRef](#)]
169. Chávez, A.M.; Solís, R.R.; Beltrán, F.J. Magnetic Graphene TiO_2 -Based Photocatalyst for the Removal of Pollutants of Emerging Concern in Water by Simulated Sunlight Aided Photocatalytic Ozonation. *Appl. Catal. B Environ.* **2020**, *262*, 118275. [[CrossRef](#)]
170. Liu, X.; Xu, J.; Ni, Z.; Wang, R.; You, J.; Guo, R. Adsorption and Visible-Light-Driven Photocatalytic Properties of $\text{Ag}_3\text{PO}_4/\text{WO}_3$ Composites: A Discussion of the Mechanism. *Chem. Eng. J.* **2019**, *356*, 22–33. [[CrossRef](#)]
171. Tang, J.; Meng, R.; Xue, Y.; Zhang, S.; Li, Q. Fabrication of a Novel $\text{Ag}_3\text{PO}_4/\text{WO}_3\cdot\text{H}_2\text{O}$ Composite with Enhanced Visible Light Photocatalytic Performance for the Degradation of Methylene Blue and Oxytetracycline. *Inorg. Chem. Commun.* **2021**, *132*, 108792. [[CrossRef](#)]
172. Li, H.; Zhang, Y.; Zhang, Q.; Wang, Y.; Fan, Y.; Gao, X.; Niu, J. Boosting Visible-Light Photocatalytic Degradation of Indomethacin by an Efficient and Photostable $\text{Ag}_3\text{PO}_4/\text{NG}/\text{WO}_3$ Composites. *Appl. Surf. Sci.* **2019**, *490*, 481–491. [[CrossRef](#)]
173. Hernández-Moreno, E.J.; Martínez de la Cruz, A.; Hinojosa-Reyes, L.; Guzmán-Mar, J.; Gracia-Pinilla, M.A.; Hernández-Ramírez, A. Synthesis, Characterization, and Visible Light-Induced Photocatalytic Evaluation of $\text{WO}_3/\text{NaNbO}_3$ Composites for the Degradation of 2,4-D Herbicide. *Mater. Today Chem.* **2021**, *19*, 100406. [[CrossRef](#)]
174. Wei, L.; Zhang, H.; Cao, J. Electrospinning of $\text{Ag}/\text{ZnWO}_4/\text{WO}_3$ Composite Nanofibers with High Visible Light Photocatalytic Activity. *Mater. Lett.* **2019**, *236*, 171–174. [[CrossRef](#)]
175. Rong, J.; Zhang, T.; Qiu, F.; Rong, X.; Zhu, X.; Zhang, X. Preparation of Hierarchical Micro/Nanostructured Bi_2S_3 - WO_3 composites for Enhanced Photocatalytic Performance. *J. Alloys Compd.* **2016**, *685*, 812–819. [[CrossRef](#)]
176. Govindaraj, T.; Mahendran, C.; Manikandan, V.S.; Archana, J.; Shkir, M.; Chandrasekaran, J. Fabrication of WO_3 Nanorods/RGO Hybrid Nanostructures for Enhanced Visible-Light-Driven Photocatalytic Degradation of Ciprofloxacin and Rhodamine B in an Ecosystem. *J. Alloys Compd.* **2021**, *868*, 159091. [[CrossRef](#)]
177. Elhakim, A.A.; El-Kemary, M.; Ibrahim, M.M.; El-Mehasseb, I.M.; El-Sheshtawy, H.S. Direct Z-Scheme of WO_3/GO Decorated with Silver Nanoparticles for Synergetic Adsorption and Photocatalytic Activity for Organic and Inorganic Water Pollutants Removal. *Appl. Surf. Sci.* **2021**, *564*, 150410. [[CrossRef](#)]
178. Gondal, M.A.; Suliman, M.A.; Dastageer, M.A.; Chuah, G.K.; Basheer, C.; Yang, D.; Suwaiyan, A. Visible Light Photocatalytic Degradation of Herbicide (Atrazine) Using Surface Plasmon Resonance Induced in Mesoporous $\text{Ag}-\text{WO}_3/\text{SBA}-15$ Composite. *J. Mol. Catal. A Chem.* **2016**, *425*, 208–216. [[CrossRef](#)]
179. Yan, L.; Hou, J.; Li, T.; Wang, Y.; Liu, C.; Zhou, T.; Jiang, W.; Wang, D.; Che, G. Tremella-like Integrated Carbon Nitride with Polyvinylimine-Doped for Enhancing Photocatalytic Degradation and Hydrogen Evolution Performances. *Sep. Purif. Technol.* **2021**, *279*, 119766. [[CrossRef](#)]

180. Zeng, X.; Liu, Y.; Xia, Y.; Uddin, M.H.; Xia, D.; McCarthy, D.T.; Deletic, A.; Yu, J.; Zhang, X. Cooperatively Modulating Reactive Oxygen Species Generation and Bacteria-Photocatalyst Contact over Graphitic Carbon Nitride by Polyethylenimine for Rapid Water Disinfection. *Appl. Catal. B Environ.* **2020**, *274*, 119095. [[CrossRef](#)]
181. Alias, N.H.; Jaafar, J.; Samitsu, S.; Yusof, N.; Othman, M.H.D.; Rahman, M.A.; Ismail, A.F.; Aziz, F.; Salleh, W.N.W.; Othman, N.H. Photocatalytic Degradation of Oilfield Produced Water Using Graphitic Carbon Nitride Embedded in Electrospun Polyacrylonitrile Nanofibers. *Chemosphere* **2018**, *204*, 79–86. [[CrossRef](#)]
182. Jing, L.; Xu, Y.; Liu, J.; Zhou, M.; Xu, H.; Xie, M.; Li, H.; Xie, J. Direct Z-Scheme Red Carbon Nitride/Rod-like Lanthanum Vanadate Composites with Enhanced Photodegradation of Antibiotic Contaminants. *Appl. Catal. B Environ.* **2020**, *277*, 119245. [[CrossRef](#)]
183. Dong, S.; Lee, G.J.; Zhou, R.; Wu, J.J. Synthesis of g-C₃N₄/BiVO₄ Heterojunction Composites for Photocatalytic Degradation of Nonylphenol Ethoxylate. *Sep. Purif. Technol.* **2020**, *250*, 117202. [[CrossRef](#)]
184. Hu, H.; Kong, W.; Wang, J.; Liu, C.; Cai, Q.; Kong, Y.; Zhou, S.; Yang, Z. Engineering 2D Compressed Layered G-C₃N₄ Nanosheets by the Intercalation of BiVO₄-Bi₂WO₆ Composites for Boosting Photocatalytic Activities. *Appl. Surf. Sci.* **2021**, *557*, 149796. [[CrossRef](#)]
185. Zhang, H.; Wei, W.; Hou, F.; Guo, W.; Zhang, Q.; Wang, T.; Wei, A. Visible-Light-Driven Photocatalytic Disinfection of *Aspergillus Fumigatus* under Germinative Biomorph: Efficiency and Mechanism. *Sep. Purif. Technol.* **2021**, *265*, 1–10. [[CrossRef](#)]
186. Iqbal, S.; Bahadur, A.; Javed, M.; Hakami, O.; Irfan, R.M.; Ahmad, Z.; AlObaid, A.; Al-Anazy, M.M.; Baghdadi, H.B.; Abd-Rabboh, H.S.M.; et al. Design Ag-Doped ZnO Heterostructure Photocatalyst with Sulfurized Graphitic C₃N₄ Showing Enhanced Photocatalytic Activity. *Mater. Sci. Eng. B Solid-State Mater. Adv. Technol.* **2021**, *272*, 115320. [[CrossRef](#)]
187. Zhang, C.; Zhang, M.; Li, Y.; Shuai, D. Visible-Light-Driven Photocatalytic Disinfection of Human Adenovirus by a Novel Heterostructure of Oxygen-Doped Graphitic Carbon Nitride and Hydrothermal Carbonation Carbon. *Appl. Catal. B Environ.* **2019**, *248*, 11–21. [[CrossRef](#)]
188. Zhou, X.; Zhang, G.; Shao, C.; Li, X.; Jiang, X.; Liu, Y. Fabrication of g-C₃N₄/SiO₂-Au Composite Nanofibers with Enhanced Visible Photocatalytic Activity. *Ceram. Int.* **2017**, *43*, 15699–15707. [[CrossRef](#)]
189. Akulinkin, A.; Bolgaru, K.; Reger, A. Facile Synthesis of Porous g-C₃N₄/β-SiAlON Material with Visible Light Photocatalytic Activity. *Mater. Lett.* **2021**, *305*, 130788. [[CrossRef](#)]
190. Jourshabani, M.; Dominic, J.A.; Achari, G.; Shariatnia, Z. Synergetic Photocatalytic Ozonation Using Modified Graphitic Carbon Nitride for Treatment of Emerging Contaminants under UVC, UVA and Visible Irradiation. *Chem. Eng. Sci.* **2019**, *209*, 115181. [[CrossRef](#)]
191. Wang, T.; Sun, M.; Sun, H.; Shang, J.; Wong, P.K. Efficient Z-Scheme Visible-Light-Driven Photocatalytic Bacterial Inactivation by Hierarchical MoS₂-Encapsulated Hydrothermal Carbonation Carbon Core-Shell Nanospheres. *Appl. Surf. Sci.* **2019**, *464*, 43–52. [[CrossRef](#)]
192. Yin, J.; Liao, G.; Zhu, D.; Lu, P.; Li, L. Photocatalytic Ozonation of Oxalic Acid by g-C₃N₄/Graphene Composites under Simulated Solar Irradiation. *J. Photochem. Photobiol. A Chem.* **2016**, *315*, 138–144. [[CrossRef](#)]
193. Ling, Y.; Liao, G.; Feng, W.; Liu, Y.; Li, L. Excellent Performance of Ordered Ag-g-C₃N₄/SBA-15 for Photocatalytic Ozonation of Oxalic Acid under Simulated Solar Light Irradiation. *J. Photochem. Photobiol. A Chem.* **2017**, *349*, 108–114. [[CrossRef](#)]